

# DISCO-DJ I: a differentiable Einstein-Boltzmann solver for cosmology

Oliver Hahn,<sup>a,b</sup> Florian List,<sup>a</sup> Natalia Porqueres<sup>c</sup>

<sup>a</sup>Department of Astrophysics, University of Vienna,  
Türkenschanzstraße 17, 1180 Vienna, Austria

<sup>b</sup>Department of Mathematics, University of Vienna,  
Oskar-Morgenstern-Platz 1, 1090 Vienna, Austria

<sup>c</sup>Department of Physics, University of Oxford,  
Denys Wilkinson Building, Keble Road, Oxford OX1 3RH, UK

E-mail: [oliver.hahn@univie.ac.at](mailto:oliver.hahn@univie.ac.at)

**Abstract.** We present the Einstein-Boltzmann module of the DISCO-DJ (DIfferentiable Simulations for COsmology – Done with JAX) software package. This module implements a fully differentiable solver for the linearised cosmological Einstein-Boltzmann equations in the JAX framework, and allows computing Jacobian matrices of all solver output with respect to all input parameters using automatic differentiation. This implies that along with the solution for a given set of parameters, the tangent hyperplane in parameter space is known as well, which is a key ingredient for cosmological inference and forecasting problems as well as for many other applications. We discuss our implementation and demonstrate that our solver agrees at the per-mille level with the existing non-differentiable solvers CAMB and CLASS, including massive neutrinos and a dark energy fluid with parameterised equation of state. We illustrate the dependence of various summary statistics in large-scale structure cosmology on model parameters using the differentiable solver, and finally demonstrate how it can be easily used for Fisher forecasting. Since the implementation is significantly shorter and more modular than existing solvers, it is easy to extend our solver to include additional physics, such as additional dark energy models, modified gravity, or other non-standard physics.

---

## Contents

<b>1</b>	<b>Introduction</b>	<b>1</b>
<b>2</b>	<b>Implementation</b>	<b>3</b>
2.1	Overview	3
2.2	Automatic differentiation	3
2.3	Stiff ODEs and implicit solvers	5
2.4	Approximation methods	6
2.5	Thermal history/recombination solver	7
<b>3</b>	<b>Validation and performance</b>	<b>7</b>
3.1	Choice of fiducial cosmological model	8
3.2	Comparison with CAMB and CLASS	8
3.3	Gradient of the power spectrum w.r.t. cosmological parameters	11
<b>4</b>	<b>Applications</b>	<b>12</b>
4.1	Redshift-space correlators for large-scale structure studies	12
4.1.1	Two-dimensional power spectrum	14
4.1.2	Correlation function multipoles	17
4.2	Fisher-forecasting with differentiable solvers	17
<b>5</b>	<b>Summary and Conclusions</b>	<b>19</b>
<b>A</b>	<b>Governing equations</b>	<b>25</b>
<b>B</b>	<b>Comparison with Class and Camb at early times</b>	<b>28</b>

---

## 1 Introduction

Describing the evolution of perturbations of Einstein’s field equations in a cosmological setting is an almost century-old quest and the foundation of inhomogeneous cosmology as much as that of all of extragalactic astrophysics. These perturbations, leading to deviations from the homogeneous Friedmann-Lemaître-Robertson-Walker (FLRW) spacetimes and the growth of structure, are described by the Einstein-Boltzmann equations, which are a set of coupled partial differential equations that describe the evolution of the energy density of the various components of the Universe along with the perturbations to the FLRW metric. First derivations of the equations date back many decades [1, 2] and subsequent revisions provide the foundation of all of modern inhomogeneous cosmology [3–5].

The Einstein-Boltzmann equations are a cornerstone of modern cosmology, and are the basis for the computation of the cosmic microwave background (CMB) anisotropies, the matter power spectrum, and other observables. The matter power spectrum, or its constituents, the individual transfer functions of the various matter components, is the starting point for all predictions of large-scale structure observables, such as the galaxy  $n$ -point spectra, weak lensing spectra, the halo mass function (in analytic models), and in particular also the initial conditions for all cosmological simulations. Building on the *linear* Einstein-Boltzmann equations, the *non-linear* evolution of structure is then typically described in the non-relativistic

collisionless limit by the Vlasov-Poisson system of equations, which is the basis for all non-linear perturbation theory and all  $N$ -body simulations (e.g. [4, 6, 7]).

Several famous software packages have been developed that integrate the linearised Einstein-Boltzmann equations. The most commonly used (historically) include the COSMICS/LINGER code [5], followed by a version specifically optimised for CMB predictions, the CMBFAST code [8], which included the line-of-sight approximation which allowed a dramatically faster computation of CMB spectra. The increasing requirements of the WMAP [9] and Planck [10] CMB missions for efficient codes have led to the highly optimised and accurate CAMB<sup>1</sup> [11] and CLASS<sup>2</sup> [12, 13] codes. Both codes feature a large number of optimizations (e.g. approximate asymptotic forms of the equations valid in various regimes, robust high-order implicit integrators), are highly optimised, and are written in compiled functional languages – FORTRAN (CAMB) and C (CLASS) – but both now have convenient PYTHON interfaces.

Both packages share a common minimal set of implemented equations (see [5, 14]), which model the evolution of cold dark matter (CDM), baryons, photons, massless and massive neutrinos, a dark energy fluid, as well as metric perturbations. While already the first codes included these energy components, CAMB and CLASS have by now been extended to include a plethora of additional models, including various dark energy and modified gravity models [15–17], and other variations such as scalar field dark matter [18, 19], early dark energy [20], and many more.

In this article, we present the Einstein-Boltzmann (EB) module of a new software package, DISCO-DJ (**D**ifferentiable **S**imulations for **C**OsMology – **D**one with **J**AX), that implements a fully differentiable Einstein-Boltzmann solver in the JAX framework [21]. This solver is based on the DIFFRAX PYTHON package [22], which (among others) implements a high-order implicit Runge-Kutta solver for stiff ordinary differential equations (ODEs). All code (including the DIFFRAX package) is built on top of the JAX framework, which provides automatic differentiation of PYTHON code, and thus allows computing the Jacobian matrix of the Einstein-Boltzmann system as well as functions of its results with respect to all input parameters. This is a key ingredient for many applications relying on gradients, including cosmological inference and the computation of the Fisher matrix computation for forecasting or optimal data compression.

In addition to differentiability, the JAX framework is also optimised for execution on graphics processing units (GPUs), which allows for a significant speed-up of the computation of the Einstein-Boltzmann system, in particular when batching over multiple cosmological models, which is an embarrassingly parallel calculation.

The current version of the EB module of DISCO-DJ (referred to as DISCO-EB in what follows) has a very lean and modular code base and is thus easy to extend and modify beyond its current minimal implementation. In particular, it is straightforward to implement additional physics, such as dark energy models, modified gravity, or other non-standard physics. The code is also easy to extend to include additional output quantities, such as e.g. the CMB anisotropies or the lensing potential. Further, the EB module will be connected to a fast  $N$ -body solver, which we are also developing as part of the DISCO-DJ package and which allows the inclusion of non-linear effects in the computation of the matter power spectrum and other key statistics and predictions for large-scale structure cosmology. We will present this in a future publication.

---

<sup>1</sup><https://camb.info>

<sup>2</sup>[https://lesgourg.github.io/class\\_public/class.html](https://lesgourg.github.io/class_public/class.html)

The structure of this article is as follows: In [section 2](#) we discuss the implementation of the Einstein-Boltzmann solver in DISCO-DJ, giving attention to differentiable solvers, implicit integrators for stiff ODEs, approximation schemes, and the thermal history solver. In [section 3](#) we validate the accuracy of the solver against the commonly used CAMB and CLASS codes. We then discuss various applications of a differentiable Einstein-Boltzmann solver, including the computation of the dependence of various summary statistics on cosmological parameters, and the computation of the Fisher information matrix in [section 4](#). Finally, we summarise and conclude in [section 5](#). An overview of the equations implemented in the Einstein-Boltzmann module of DISCO-DJ is given in [Appendix A](#).

## 2 Implementation

In this section, we discuss aspects of the implementation of the linear Einstein-Boltzmann module of DISCO-DJ.

### 2.1 Overview

The Einstein-Boltzmann equations are a set of non-linear coupled partial differential equations that describe the evolution of the energy density of the various components of the Universe along with the perturbations to the FLRW metric. A fully self-consistent non-linear solution all the way to late times and small scales is however so far computationally untractable (but see [\[23\]](#) for a second-order EB solver). Instead, in cosmology, one typically splits the evolution into a linear and a non-linear part. The linear part is described by the linearised Einstein-Boltzmann equations. The non-linear part is typically described in the non-relativistic collisionless limit by the Vlasov-Poisson system of equations, which is solved with  $N$ -body methods (e.g. [\[7\]](#)), using input from the linear Einstein-Boltzmann solver.

In this work, we focus on the linear Einstein-Boltzmann equations including CDM, baryons, photons, massive and massless neutrinos, and clustering dark energy. The governing equations are stated in full in [Appendix A](#) for reference. The same equations are also implemented in the popular CAMB and CLASS solvers. Those solvers also include additional physical models (e.g. early dark energy, dark radiation, etc.) that we do not include (yet).

The new aspect of our work is that we implement the Einstein-Boltzmann equations in the JAX framework, which allows us to compute the Jacobian matrix of the Einstein-Boltzmann system (which is crucial input for implicit ODE solvers) as well as of any function of its results with respect to all parameters. For this reason, in this article, we first discuss the aspect of automatic differentiation in [subsection 2.2](#) below. The linearised Einstein-Boltzmann equations are so-called ‘stiff’ coupled ODEs, which are most efficiently solved by implicit integrators, an aspect we discuss in [subsection 2.3](#). Solvers such as CAMB and CLASS employ a number of numerical approximation schemes in order to reduce the large number of equations needed to be solved and optimise the time-to-result for a given precision. We discuss these aspects in [subsection 2.4](#). Finally, we also discuss our choice of thermal history solver and its performance in [subsection 2.5](#).

### 2.2 Automatic differentiation

The autodiff paradigm [\[24\]](#) has seen rapidly increasing interest recently due to the machine learning revolution. Traditionally, the computer-aided computation of derivatives could be subdivided into *symbolic* and *numerical* differentiation methods. Symbolic differentiation involves algorithmically determining the derivative of a function as a new symbolic expression

by applying differentiation rules such as the chain rule, the product rule, etc. This approach is implemented in software packages such as the popular MATHEMATICA program [25] and the PYTHON module SYMPY [26]. While these programs are often able to find surprisingly simple expressions for derivatives that would be hard to compute by hand, more complex functions may result in lengthy expressions that are far from computationally optimal when being evaluated with concrete numerical values. On the other hand, numerical differentiation relies on finite difference approximations of derivatives. This introduces a hyperparameter, namely the step size, upon which the results can depend sensitively. In particular, numerical approximations of higher derivatives are oftentimes simply too noisy to be useful in practice.

More recently, the autodiff paradigm (also known as *automatic* differentiation) has become a popular third contender among computational differentiation methods and is now the de-facto standard in the field of machine learning. Automatic differentiation exploits the fact that programs perform the evaluation of any mathematical function of some inputs as a nested sequence of simple functions such as summation, multiplication, exponentiation, etc. The derivative of each of these building blocks is known, so when the program sequentially propagates the inputs through these blocks, the derivative information can be passed on alongside the computed values simply by using the chain rule. This particular flavour of autodiff is known as forward-mode differentiation. Alternatively, if the chain rule is instead performed starting at the outputs of the function and propagating backwards to the inputs, one obtains reverse-mode differentiation. Which of the two is computationally cheaper mainly depends on the dimensionality of the inputs and outputs (backward-mode for many inputs  $\mapsto$  few outputs, e.g. when computing a scalar loss function w.r.t. the millions of parameters of a neural network, forward-mode for few inputs  $\mapsto$  many outputs, e.g. when differentiating a field quantity w.r.t. a cosmological parameter). Keeping track of the derivatives with autodiff only entails a constant computational overhead for each of the function’s building blocks.

In our case, the quantity of interest, namely the matter power spectrum  $P$ , is obtained as the solution of a system of differential equations, specifically the cosmological Einstein-Boltzmann equations. Thus, the computation of gradients such as  $\partial P/\partial\Omega_m$  requires us to differentiate through the solution of the differential equations. This can be done in two different ways: (1) differentiate iteratively through the time steps performed by the numerical solver (“discretise-then-optimise” approach) or (2) set up a continuous “adjoint equation” for  $\partial P/\partial\Omega_m$  that then must be solved backwards in time, also with a numerical method (“optimise-then-discretise” approach).<sup>3</sup> Generally, the optimise-then-discretise approach yields less accurate derivatives because the numerical discretisation of the backwards-in-time equations required for the computation of the derivatives is not synchronised with that for the forward-in-time equations for the quantities themselves [27]; however, it is more memory-efficient than its discretise-then-optimise counterpart.

In this work, we rely on Google’s array-based autodiff PYTHON library JAX [21]. JAX conveniently allows writing differentiable programs in high-level PYTHON that are then compiled just-in-time (JIT) to execute efficiently on graphics or tensor processing units (GPUs, TPUs), making use of the fast XLA (Accelerated Linear Algebra) compiler. Syntactically, much of JAX follows the syntax of NUMPY, making it easy for users with PYTHON experience to switch from plain NUMPY (which runs on central processing units, i.e. CPUs,

---

<sup>3</sup>Instead of the power spectrum itself, one could similarly differentiate a *loss function* that gauges the match between the computed power spectrum  $P$  and an observation  $P_{\text{obs}}$  w.r.t. the cosmological parameters, which is a typical scenario in the context of parameter inference.

and is neither compiled nor differentiable) to JAX. It supports forward- and reverse-mode differentiation, the computation of higher-order derivatives such as Hessian matrices, holomorphic differentiation, and the vectorised computation of derivatives, among other useful features. The JAX ecosystem is steadily expanding, and there exist JAX-based packages for machine learning (e.g. [28]), for physics simulations (e.g. [29]), probabilistic programming (e.g. [30, 31]), and many other applications, which can be integrated seamlessly with custom JAX code. Importantly, we use the JAX-based DIFFRAX library for solving differential equations [22], which supports different flavours of “discretise-then-optimise” and “optimise-then-discretise” derivatives. The current version of DISCO-EB supports both forward (via DIFFRAX’s `DirectAdjoint`) and backward (via DIFFRAX’s `BacksolveAdjoint`) differentiation. Other differentiable frameworks exist, notably e.g. BOLT<sup>4</sup> implements a forward-differentiable Einstein-Boltzmann solver in JULIA (but is unpublished at the time of writing).

In the past few years, JAX has garnered considerable interest in the cosmology community. For example, Ref. [32] presented a differentiable cosmology library using JAX, Ref. [33] introduced a JAX-based inference framework for cosmology, and the  $N$ -body code by Ref. [34] is fully differentiable thanks to its implementation in JAX. It has also been used in the context of estimating weak lensing shear [35] and for modelling the evolution of dark matter haloes [36].

### 2.3 Stiff ODEs and implicit solvers

The Einstein-Boltzmann equations, cf. Appendix A, are a stiff system of ODEs due to the multiple time scales involved in the various physical processes, which makes them ill-suited for explicit time integration schemes [37]. Various approximations can be employed (cf. [13], and subsection 2.4) to reduce the stiffness of the system (see also [38]), but these approximations are generally not valid for the entire domain of integration. State-of-the-art solvers therefore use a combined approach of approximation schemes and a powerful high-order implicit time integration scheme [13, 39]. A main draw-back of implicit solvers is that the Jacobian matrix of the system needs to be computed and inverted at each time step, which is computationally expensive, particularly so for large systems such as the cosmological Einstein-Boltzmann equations.

A main advantage of the autodiff paradigm is that the Jacobian matrix of the system can be computed automatically without specifying it explicitly or having to recourse to finite-difference approximations. For DISCO-EB, we adopt the DIFFRAX package [22] for this purpose, which comes with various high-order implicit and explicit integration and is also built on top of the JAX framework. Specifically, we adopt the highest order implicit solver implemented in DIFFRAX: the 7-stage KVAERNO5 solver [40], a singly diagonally implicit Runge-Kutta (ESDIRK) method of order 5/4. We note that while CLASS uses sparse storage for the Jacobian, sparse matrix operations in JAX are still in an experimental stage and thus, DIFFRAX does not (yet) support sparse matrices. Instead, we use the JAX `vmap` function to vectorise the computation of multiple modes on the GPU.

After linearisation of the Einstein-Boltzmann system [5], the equations for individual wave numbers  $k$  decouple in Fourier space and can thus be solved individually. The resulting Jacobian for multiple wave numbers thus has a block-diagonal structure. Since such sparse Jacobian matrices can currently not be handled, an optimised joint integration of multiple

---

<sup>4</sup><https://github.com/xzackli/Bolt.jl>

wave numbers, which leads to a block diagonal Jacobian (since the different modes do not couple), is currently not possible. Storing the full Jacobian is computationally prohibitive. While we are, therefore, currently restricted to integrating mode-by-mode in an embarrassingly parallel way, there is plausibly room for future performance improvements along such lines. In applications where the Einstein-Boltzmann system needs to be solved for multiple sets of cosmological parameters, e.g. in the context of inference tasks, it is straightforward to batch the computation over those sets in order to increase the computational speed, harnessing the highly parallel architecture of GPUs.

## 2.4 Approximation methods

In order to speed up the integration of the Einstein-Boltzmann system, for CLASS and CAMB, it has been critical to employ various approximation schemes [13, 39] in order to reduce the number of degrees of freedom of the high-dimensional system and to reduce the stiffness of the system. The situation is somewhat different for GPU-JAX-based solvers. While the Jacobian matrix of the system can be computed automatically (which is, in fact, more efficient than a finite difference calculation), the computation of the Jacobian matrix is still computationally expensive, and it is still desirable to reduce the number of degrees of freedom of the system. However, adaptively switching to a reduced set of variables based on a predefined criterion introduces additional algorithmic complexity, which is not desirable in the context of GPU-based solvers. Specifically, we found that neither of the commonly used approximation schemes yielded a  $\mathcal{O}(1)$  performance improvement, and, while we implemented the tight coupling approximation [5, 13] (valid when the baryons are fully ionised and tightly coupled to the photons), and all the approximations used in CLASS [13] (notably the ultra-relativistic fluid approximation, applying to massless neutrinos at late times, as well as the radiation streaming approximation, applying to massless neutrinos and photons at even later times) in DISCO-EB, we do not currently use any of them.

A main performance bottleneck lies in the computation of the Jacobian matrix, which scales quadratically with the number of equations (see Appendix A). The number of equations scales with the number  $\ell_{\max}$  of the multipole where the photon and neutrino distribution functions are truncated, and the number of massive neutrino mass bins. Specifically we have

$$8 + 2 \times \ell_{\gamma, \max} + \ell_{\nu \text{UR}, \max} + n_q \times \ell_{\nu \text{massive}, \max} \quad (2.1)$$

equations. The ‘8’ entails the equations for metric+CDM+baryon+dark energy perturbations,  $\ell_{\gamma, \max}$  is the maximum multipole moment of the photon distribution function,  $\ell_{\nu \text{UR}, \max}$  is the maximum multipole moment of the massless neutrino distribution function,  $n_q$  is the number of neutrino momentum bins, and  $\ell_{\nu \text{massive}, \max}$  is the maximum multipole moment of the massive neutrino distribution function.

A key optimisation, therefore, lies in a clever choice of neutrino momentum bins so that  $n_q$  can be chosen as small as possible. Specifically, [41] found that a 3-5 bin Gauss-Laguerre inspired integral approximation used by CAMB (see Appendix A of [41]) works very well in this context. The neutrino momentum bins are chosen so that the following integral is well approximated by a sum over the bins

$$\frac{1}{4} \int_0^\infty dq \frac{q^4 e^q}{(1 + e^q)^2} v^w \nu_\ell \approx \sum_i K_i v^w \nu_\ell, \quad (2.2)$$

where  $q$  is the neutrino momentum,  $v$  is the (relativistic) neutrino velocity,  $\nu_\ell$  is a rescaled function of the  $\ell$ -th multipole moment of the neutrino distribution function,  $w = -1, 0, 1$

(depending on which moment of the distribution function is to be computed, cf. eqs. (55) of [5]), and  $K_i$  are the kernel weights approximating the integral. The authors of [41] propose the following very accurate binning schemes:

$$\begin{aligned}
\text{3-point:} & & q &= (0.913201, 3.37517, 7.79184), \\
& & K &= (0.0687359, 3.31435, 2.29911), \\
\text{4-point:} & & q &= (0.7, 2.62814, 5.90428, 12), \\
& & K &= (0.0200251, 1.84539, 3.52736, 0.289427) \\
\text{5-point:} & & q &= (0.583165, 2.0, 4.0, 7.26582, 13.0), \\
& & K &= (0.0081201, 0.689407, 2.8063, 2.05156, 0.12681)
\end{aligned}$$

The truncation of the neutrino Boltzmann hierarchy  $\ell_{\nu, \text{max}} = \text{lnumax}$  then determines the number of equations that need to be solved as the product of  $\text{lnumax}$  and the number of neutrino momentum bins. When neutrinos are sufficiently non-relativistic,  $\text{lnumax}$  can, in principle, be reduced to a very small number (2 or 3, cf. [41]).

For our first proof-of-concept version of DISCO-EB, we decided to leave out all such further approximations, but we expect that a possible factor of 2-3 in speed could be gained by a careful evaluation of the various approximation schemes on integration of the ODEs on GPUs (specifically optimizing how to best change the number of equations integrating directly in the integrator). We leave this for future work.

## 2.5 Thermal history/recombination solver

Currently, we adopt a simplified thermal history solver in DISCO-DJ, that is based on the original RECFAST model [42]. The original implementation of the thermal history in COSMICS (Section 5.8 of [5], which is based on [43] with addition Helium) is not accurate enough to obtain sub-per-cent-level agreement with CAMB or CLASS. All state-of-the-art Einstein-Boltzmann solvers employ at least RECFAST [42], or the newer COSMOREC [44] and HYREC [45] (which has been further developed into HYREC2 [46]) solvers. We found however that, since we are predominantly interested in the matter power spectrum and late times (rather than a CMB spectrum), adopting the original RECFAST model is accurate enough for our purposes. While the thermal history solver is thus not the main source of error in the late time matter power spectrum, we are planning to eventually add a more accurate recombination solver in DISCO-DJ. The current version implements the original RECFAST model, that we dub ‘RECFASTmini’, as well as the much older MB95 model [5].

In Figure 1, we compare the ionization history of the baseline cosmology computed using the simplified models in DISCO-EB with the RECFAST and HYREC solvers interfaced in CLASS. The main difference is due to the different treatment of the helium recombination, with a longer phase of  $\text{He}^+$  recombination in RECFAST. As we will show below, for late times  $z \lesssim 1000$ , the simplified ‘RECFASTmini’ model is sufficient to reach agreement of late time spectra with CLASS or CAMB to below one per cent.

## 3 Validation and performance

We next validate the performance of our solver against the CAMB and CLASS solvers. First, we compare the precision of our solver for a given set of cosmological input parameters. Second, we demonstrate that our solver is able to compute the Jacobian matrix of the system



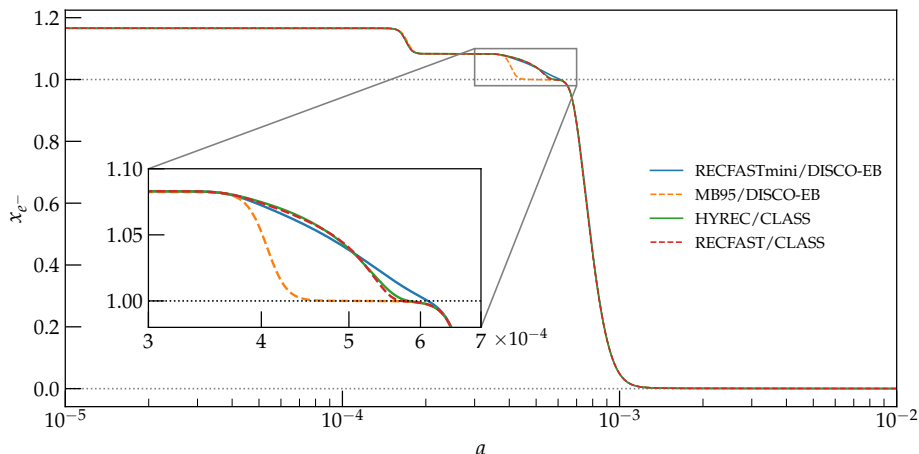


**Figure 1:** Performance of the simplified recombination solver ‘RECFASTmini’ in DISCO-DJ in comparison with the more accurate RECFAST and HYREC solvers used in CLASS, and the original MB95 model [5] (also available in DISCO-DJ). We show the ionization fraction  $x_{e-}$  as a function of the scale factor  $a$  for the baseline cosmology computed using the simplified model based on the original RECFAST (blue), the much older MB95 model (orange dashed), as well the most recent RECFAST (red dashed) and HYREC (green) modules in CLASS. The main difference is due to details in the treatment of the combined hydrogen-helium recombination. None of these differences (except MB95) have a measurable effect late-time on matter components.

with respect to all input parameters, and validate the correctness of the Jacobian matrix by comparing it to finite-difference approximations.

### 3.1 Choice of fiducial cosmological model

For all comparisons, unless otherwise indicated, we adopt a flat (extended)  $\Lambda$ CDM cosmology, with the cosmological parameter set shown in Table 1, which is consistent with the PLANCK 2018 EE+BAO+SN constraints [47]. Specifically, we consider the standard extension with inclusion of one massive neutrino, along with a dark energy fluid with parameterised (Chevallier-Polarski-Linder) equation of state  $w = p/\rho = w_0 + w_a(1 - a)$ . We adopt  $w_0 = -0.99$  instead of  $-1$  since derivatives w.r.t.  $w_0$  are defined only in the one-sided limit at  $w = -1$ , a complication we thus avoid (although defining one-sided derivatives is, in principle, also supported by JAX).

### 3.2 Comparison with CAMB and CLASS

In this subsection, we validate the performance of the DISCO-DJ Einstein-Boltzmann solver against the well-established and commonly used CAMB<sup>6</sup> [11], specifically version 1.5.0, and CLASS<sup>7</sup> [12], version 3.2.0, software packages. We use both codes via their PYTHON interfaces.

Since DISCO-DJ is aimed at large-scale structure studies, we are mainly interested in the post-recombination regime. We use high accuracy settings for all three codes, listed

<sup>5</sup>Note that we modified this from  $-1$  as solutions are only one-sidedly differentiable at  $w_0 = -1$ .

<sup>6</sup>Available from <https://camb.info>

<sup>7</sup>Available from [https://lesgourg.github.io/class\\_public/class.html](https://lesgourg.github.io/class_public/class.html)

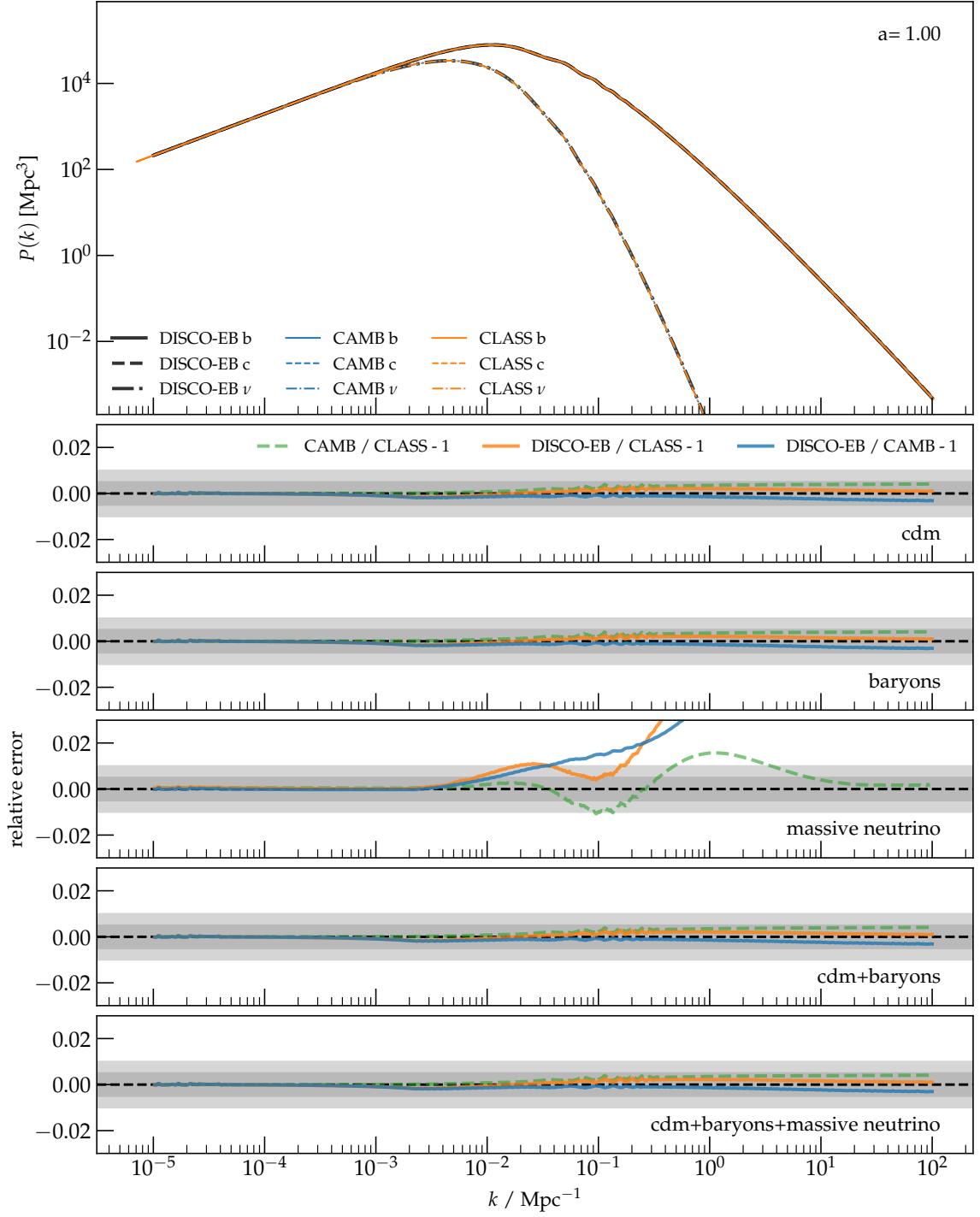


**Figure 2:** Comparison at  $a = 1$  of the performance of our differentiable Einstein-Boltzmann solver vs. CAMB and CLASS. The top panel shows the power spectrum of density perturbations in baryons (solid), CDM (dashed), and the 0.06 eV massive neutrino (dot-dashed). The lower panels indicate the relative errors  $P/P_{\text{ref}} - 1$  for CDM, baryons, massive neutrinos, CDM+baryons, and total matter = CDM+baryons+massive neutrino. The grey bands indicate 1 per cent deviation (light grey) and 0.5 per cent deviation (darker grey). All EB solvers were run on high-accuracy settings for this comparison, but we note that it might well be possible to improve agreement further with other parameter choices.

Parameter	Value	Meaning
$\Omega_k$	0.0	curvature density parameter (constraint)
$\Omega_b$	0.0488911	baryon density parameter
$\Omega_m$	0.3099	matter density parameter
$h$	0.67742	Hubble parameter
$n_s$	0.96822	primordial spectral index
$A_s$	$2.1064 \times 10^{-9}$	amplitude at $k_p = 0.05 \text{ Mpc}^{-1}$
$N_{\text{eff}}$	3.046	effective number of ultrarelativistic species
$m_\nu$	0.06 eV	mass of neutrino
$w_0$	-0.99	dark energy equation of state parameter <sup>5</sup>
$w_a$	0.0	dark energy equation of state parameter
$c_a^2$	1.0	dark energy sound speed
$Y_{\text{He}}$	0.248	primordial Helium fraction
$T_{\text{CMB}}$	2.7255 K	CMB temperature today

**Table 1:** Baseline flat PLANCK2018 EE+BAO+SN cosmological parameters used for all tests unless otherwise indicated. The dark energy density  $\Omega_{\text{DE}}$  is chosen so that all densities add up to critical and thus  $\Omega_k = 0$  serves as a constraint, not a parameter.

```

AccuracyBoost = 3
lAccuracyBoost = 3
DoLateRadTruncation = False
MassiveNuMethod= 'Nu_int'
Transfer.high_precision = True
Transfer.accurate_massive_neutrino_transfers = True
Reion.Reionization = False

```

**Table 2:** Parameters used for the reference high-precision CAMB runs.

```

l_max_g = 64
l_max_pol_g = 64
l_max_ur = 64
l_max_ncdm = 64
use_ppf = no
radiation_streaming_approximation = 3
ncdm_fluid_approximation = 3
ur_fluid_approximation = 3
reio_parametrization = reio_none

```

**Table 3:** Parameters used for the reference high-precision CLASS runs. Note that for DISCO-EB, we used only  $\ell_{\text{max}} = 32$ .

in [Table 2](#) and [Table 3](#), for CAMB and CLASS respectively, to boost the accuracy of the integration results. For DISCO-EB, we adopted a maximum  $\ell$  of the hierarchy truncation of 32, as well as the 5-point neutrino momentum integration. Note that we found that CLASS enables by default some optimizations which lead to relatively large differences, notably we had to disable some optimizations for massive neutrinos and the dark energy fluid.

In all tests, we employ the cosmological parameters listed in [Table 1](#) as our baseline cosmological model and compute the evolution from adiabatic (isentropic) initial conditions using DISCO-EB, CAMB, and CLASS. We compare the resulting power spectra for baryons, CDM, the massive neutrino, as well as the combined total matter (CDM+baryon+massive neutrino) and the ‘ $b + c$ ’ (baryon+CDM) spectra to those obtained from CAMB and CLASS at  $z = 0$  in [Figure 2](#).

In all cases, we find excellent agreement between the three codes, with relative differences of at most a few per mille for all quantities of interest, with the sole exception of the massive neutrino perturbations. Generally the difference is similar w.r.t. both CLASS and CAMB. While all three codes use high precision settings, it is slightly surprising that the massive neutrino spectra do not agree better. Clearly however, the difference is largest for DISCO-EB, but we haven’t found the reason for the differences yet. In practice, these differences are not significant for the matter power spectrum, since they appear in the free-streaming suppressed part of the massive neutrino perturbations.

A similar comparison at  $z = 99$  ( $a = 10^{-2}$ ) (shown in [Figure 8](#) in the appendix) yields very similar results with few per-mille differences in all perturbations. Slightly larger differences exist for baryons, presumably due to differences in the recombination solver used. To improve agreement even further at higher  $z$ , we would therefore have to improve the quality of the recombination solver, which we leave for future work (see discussion in [subsection 2.5](#)). Again, larger differences exist for massive neutrinos in the free-streaming suppressed regime, which are however not of great importance.

All in all, the agreement is therefore excellent, and we conclude that DISCO-EB is able to reproduce the results of CAMB and CLASS to few per mille accuracy for all quantities of interest. We caution that differences between the results of CAMB and CLASS might still be reduced by more optimal parameter choices.

### 3.3 Gradient of the power spectrum w.r.t. cosmological parameters

Having a fully differentiable Einstein-Boltzmann solver permits taking derivatives with respect to any parameter of the model. In this subsection, we demonstrate this capability by computing the Jacobian matrix of the total matter (CDM+baryon+massive neutrino) density power spectrum at fixed time ( $a = 1$ ) with respect to all cosmological model input parameters. This is achieved by wrapping the power spectrum calculation in a JAX function, which takes the parameters as an argument, and then calls the `jacfwd` method of the JAX library. Specifically, let  $\boldsymbol{\vartheta} \in \mathbb{R}^n$  be the vector of cosmological model input parameters, where  $n = 12$  for our baseline cosmology (see [Table 1](#)), and specifically

$$\boldsymbol{\vartheta} = (H_0, \Omega_m, \Omega_b, N_{\text{eff}}, m_\nu, T_{\text{CMB}}, Y_{\text{He}}, A_s, n_s, w_0, w_a, c_a^2)^\top. \quad (3.1)$$

In principle, all physical constants and other parameters, including e.g. numerical parameters, could be added here. Let  $P(k, a | \boldsymbol{\vartheta})$  be the vector of power spectrum values at fixed time, then we are interested in computing the logarithmic Jacobian

$$\mathbf{J}_\boldsymbol{\vartheta} := \nabla_{\boldsymbol{\vartheta}} \log P(k, a | \boldsymbol{\vartheta}). \quad (3.2)$$

The result of the autodiff computation is shown in [Figure 3](#) as a solid black line. The respective component of the Jacobian is indicated by a label in each plot. For comparison, we also show the finite-difference approximation of the Jacobian computed with CAMB and

CLASS (note that we have adopted  $\ell_{\max} = 32$  for CLASS in this case). Specifically, we compute the finite difference approximation of the Jacobian as

$$J_{\vartheta_i}^{\text{FD}} = \frac{\log P(k, a | \boldsymbol{\vartheta} + \frac{\epsilon}{2}\vartheta_i \mathbf{e}_i) - \log P(k, a | \boldsymbol{\vartheta} - \frac{\epsilon}{2}\vartheta_i \mathbf{e}_i)}{\epsilon \vartheta_i} + \mathcal{O}(\epsilon^2), \quad (3.3)$$

which means that for second-order finite differences two calls to the EB solver are needed per model parameter. We show the results for  $\epsilon = 10^{-2}$  in [Figure 3](#). The top panel in each case represents the value of the derivative as a function of the wave number, while the bottom panel shows the relative difference between the DISCO-EB autodiff computation and the finite difference solutions using CAMB and CLASS.

We note that the autodiff evaluation and the finite difference approximation agree generally very well to mostly better than one per cent. We found that this requires  $\epsilon \approx 10^{-2}$ , while for smaller values, the finite difference estimates become very noisy. Nonetheless, where visible, the autodiff version shows fewer signs of numerical artefacts. The only significant difference is found for the neutrino mass derivative, which is slightly offset between autodiff and finite difference. We have not found a reason for this discrepancy yet. We note that the finite difference approximation is computationally expensive, since it requires two calls to the EB solver per parameter, while the autodiff computation is computationally much cheaper. Due to the large impact of optimizations and specific parameter choices on the performance of the EB solvers, we prefer to refrain from a detailed comparison of the computational performance of the autodiff and finite difference approaches.

Finally, in [Figure 4](#), we show full time and space dependence of the derivative of the total matter power spectrum (cdm+baryons+massive neutrino) w.r.t. the model parameters. Each panel shows the colour-coded change in the power spectrum, with red colours indicating an increase and blue a decrease, as a function of scale factor ( $y$ -axis) and wave number ( $x$ -axis). A white colour indicates that the respective parameter has no impact on the matter power spectrum at that time and scale. For this analysis, we extend this (qualitative) analysis to earlier times ( $a = 10^{-5}$ ) revealing how the BAO feature propagates to increasingly larger scale prior to decoupling at  $a \approx 10^{-3}$ . Also intuitively, the neutrino mass dependence clearly shows when the neutrino becomes non-relativistic at  $z \lesssim 100$ , while the signature of the dark energy EOS parameters  $w_0$ ,  $w_a$  and  $c_a^2$  is restricted to very late times  $z \lesssim 1$ , with  $c_a^2$  clearly impacting only the sound horizon in the dark energy fluid.

## 4 Applications

In this section, we demonstrate a few applications of the differentiable Einstein-Boltzmann solver. We note that these are not meant to be exhaustive in any way. Specifically, two main applications of a differentiable solver will be for parameter inference and the construction of emulators, aspects that we postpone to future work. Nonetheless, the cases we highlight here are meant to demonstrate the easy applicability and integration of the solver for a range of applications relevant to large-scale structure cosmology.

### 4.1 Redshift-space correlators for large-scale structure studies

The matter power spectrum itself is not directly observable but can be constrained e.g. through the clustering of galaxies. Galaxies are, however, biased tracers of the underlying matter distribution (cf. [\[48\]](#) for a review) and their three-dimensional distribution can generally only be determined in redshift space [\[49\]](#). As a next proof-of-concept test, we demonstrate

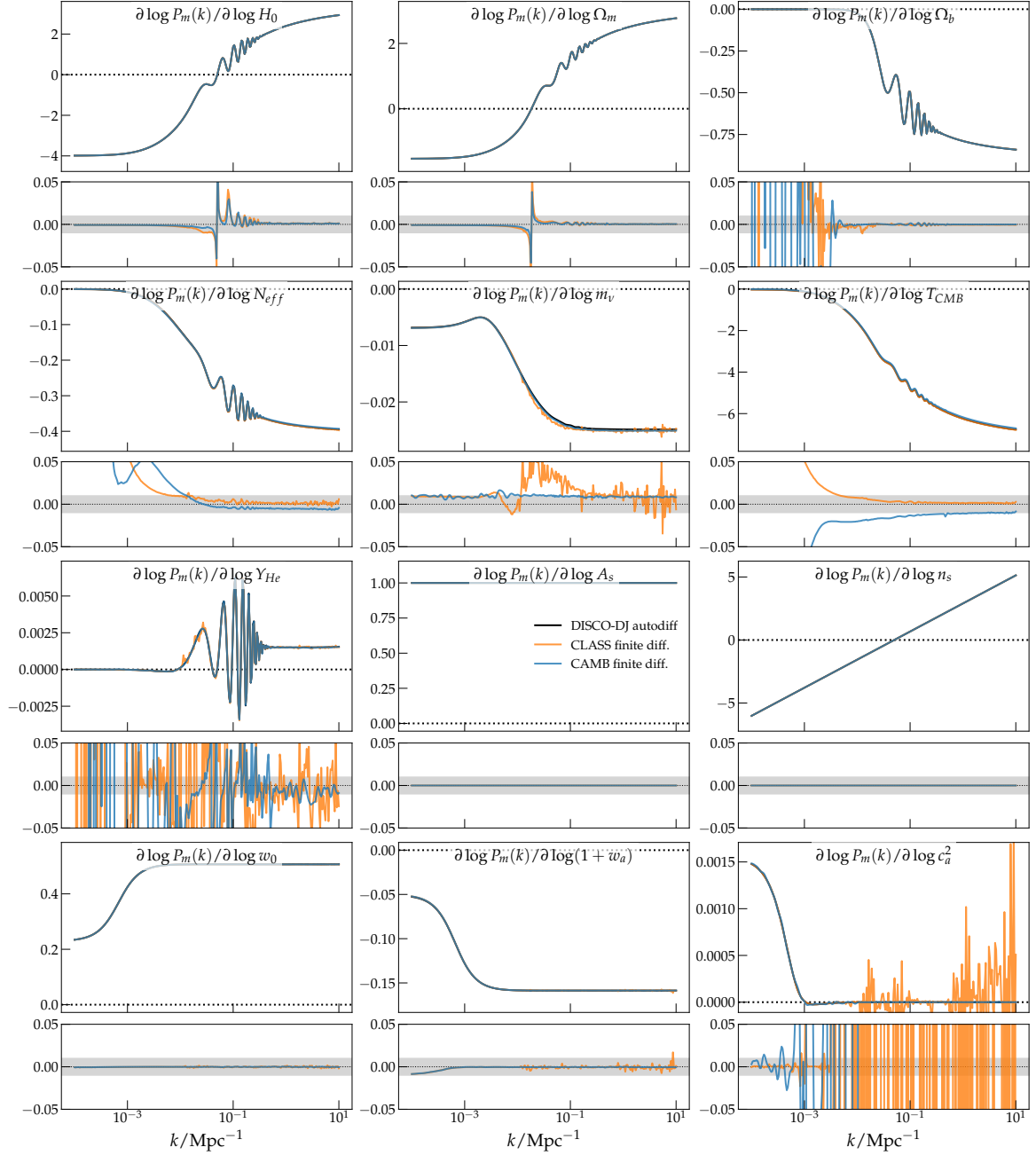


**Figure 3:** Derivative of the total matter (CDM+baryon+massive neutrino) density power spectrum at fixed time ( $a = 1$ ) with respect to all cosmological model input parameters, evaluated at the fiducial parameter values. We show the result of the DISCO-EB autodiff computation (black) and a second-order finite-difference approximation based on CLASS (orange) and CAMB, computed using eq. (3.3) with  $\epsilon = 10^{-2}$ . The respective derivative is indicated by a label in each plot. The top panel in each case represents the value of the derivative as a function of the wave number, while the bottom panel shows the relative difference between the DISCO-EB autodiff computation and the finite difference solutions.

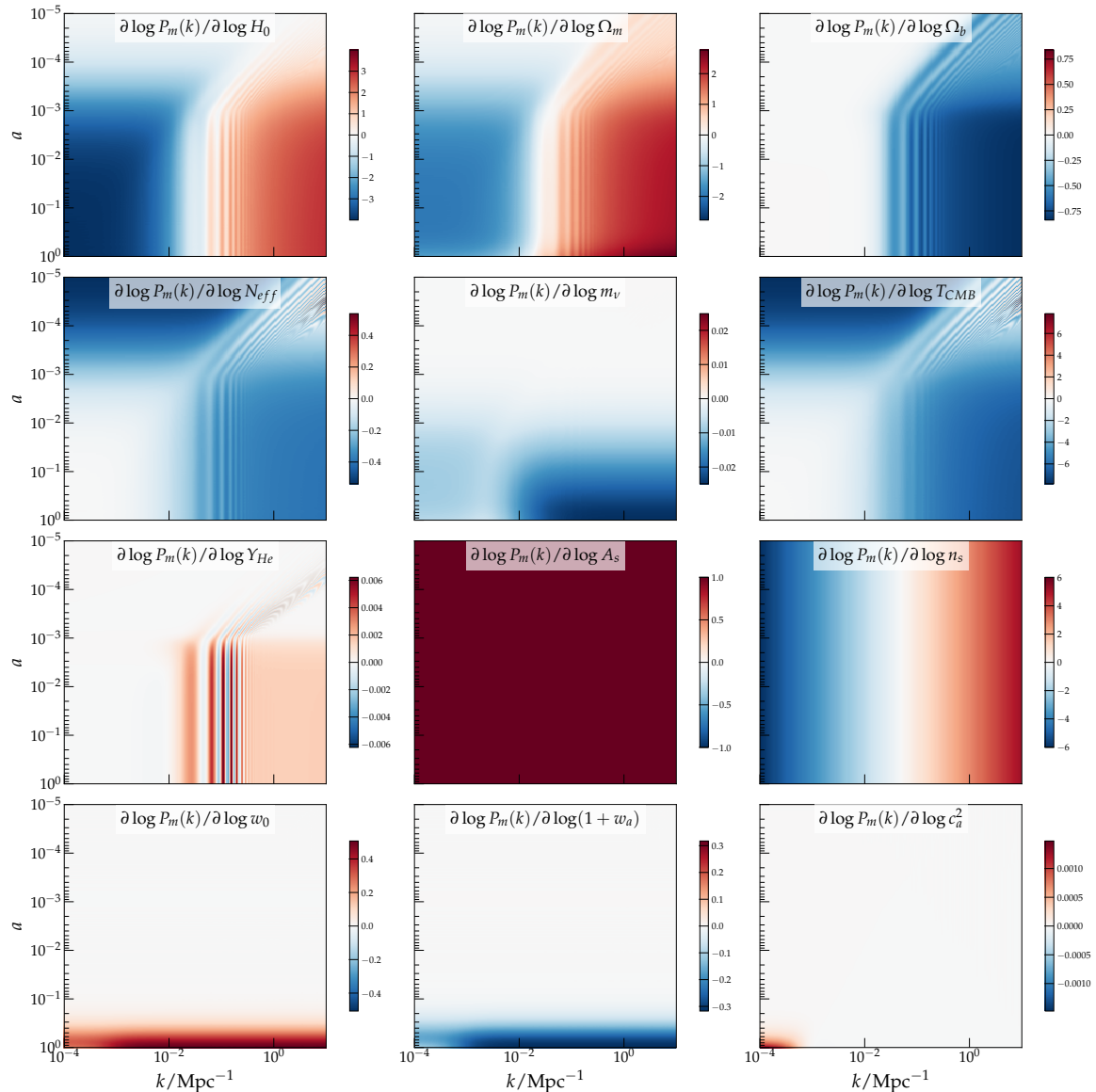


**Figure 4:** Time and spatial dependence of the logarithmic derivative of the total matter power spectrum w.r.t. the cosmological parameters. Each panel shows the colour-coded change in the power spectrum in arbitrary normalisation, with red indicating an increase and blue a decrease w.r.t. an arbitrary baseline, as a function of scale factor ( $y$ -axis) and wave number ( $x$ -axis). Compare with [Figure 3](#) which represents a slice at fixed time  $a = 1$ .

a differentiable calculation of the redshift-space power spectrum and the correlation function multipoles of biased tracers, as this is a common input for large-scale structure studies.

#### 4.1.1 Two-dimensional power spectrum

The proper motions  $v_{\parallel}$  of galaxies parallel to the line-of-sight (LOS) contribute to the measured redshift

$$1 + z_{\text{obs}} = (1 + z_{\text{cosmo}}) (1 + v_{\parallel}/c) \quad (4.1)$$

and lead to the redshift space distortion (RSD) effect. At linear order and in the Newtonian limit, the redshift-space power spectrum can be computed from the matter power spectrum using the Kaiser formula [49]. For linearly biased tracers with density contrast  $\delta_g$  it states that

$$\delta_g^{\text{Kaiser}} = b \delta_m - \mu^2 \frac{\theta_m}{\mathcal{H}}, \quad (4.2)$$

where  $b$  is the linear bias coefficient (which we fix to  $b = 2$  here),  $\mu := \cos \alpha$  for an angle  $\alpha$  between  $\mathbf{k}$  and the line-of-sight,  $\theta_m$  is the matter velocity divergence, and  $\mathcal{H} = a'/a$  is the conformal-time expansion rate. Further, one needs to assume an irrotational velocity field ( $\mathbf{v} = \nabla \nabla^{-2} \theta$ ) and the absence of velocity bias (i.e. galaxy velocity  $\theta_g = \theta_m$ ) for this relation to hold. Commonly, the growth rate  $f$  is used to express  $\theta_m$  in terms of  $\delta_m$ , but since we have both fields from the EB solver, it is more convenient to work directly with the velocity divergence. The fields  $\delta_m$  and  $\theta_m$  are readily obtained from DISCO-EB. Following [50], we account for uncertainty in the observed redshift  $z_{\text{obs}}$  with the Gaussian dispersion kernel (cf. [51, 52])

$$F_z(k, \mu; z) = \exp\left(-\frac{c^2 k^2}{\mathcal{H}^2} \mu^2 \sigma_{z,0}^2\right) \quad (4.3)$$

where  $\sigma_{z,0}(1+z) = \sigma_z$  is the measurement error on the redshift (we adopt  $\sigma_{z,0} = 0.03$  as the fiducial value). We thus arrive at a linear model for the observed redshift-space power spectrum – which includes effective bias, redshift space anisotropy, and redshift errors – of the form

$$P_{\text{obs}}(k, \mu; z) = \left[ b \delta_m(k; z) - \frac{\mu^2}{\mathcal{H}} \theta_m(k; z) \right]^2 F_z(k, \mu; z). \quad (4.4)$$

Note that from this point onwards, we omit the explicit dependence of the power spectrum on  $\mathcal{V}$  in the notation.

In Figure 5, we show the logarithmic gradients of the observed matter power spectrum  $\partial \log P_{\text{obs}} / \partial \log \vartheta_i$  with respect to a key subset of model parameters  $\mathcal{V}$  as obtained with DISCO-DJ. Wave vectors parallel to the LOS are indicated in the  $0^\circ$  direction, while modes perpendicular are at  $90^\circ$  and  $270^\circ$ . The radial coordinate is  $\log k$ , which is clipped to be between  $k_{\text{min}} = 10^{-4} \text{ Mpc}^{-1}$  (the center point) and  $k_{\text{max}} = 10 \text{ Mpc}^{-1}$  (the outer circle). The colour scale indicates a positive dependence of  $P_{\text{obs}}$  on the parameter (red) or a negative dependence (blue). A white region indicates that the information content due to parameter  $\vartheta_i$  of the power spectrum vanishes. These plots all have an ‘eye’-shaped appearance, which is due to the fact that the photo- $z$  error term  $F_z$  causes an exponential loss of information for large  $k$  for  $\mu \approx 0, \pi$ , i.e. for modes parallel to the LOS, while much smaller scales (larger  $k$ ) can be probed perpendicular.

A few aspects are notable. First, the BAO feature is clearly visible in the derivatives w.r.t.  $\Omega_b$ ,  $N_{\text{eff}}$ ,  $Y_{\text{He}}$ , and to a lesser extent  $\Omega_m$ , indicating that these parameters have a strong impact on the BAO feature (i.e. causing a shift in the BAO scale). Secondly, the derivatives w.r.t.  $H_0$  and  $m_\nu$  have the strongest impact on the photo- $z$  cutoff scale, which is expected since these parameters have the strongest impact on the expansion rate  $\mathcal{H}$  and thus determine the scale of information loss for given photo- $z$  uncertainties. Thirdly, the derivatives w.r.t.  $\Omega_m$  and the bias parameter  $b$  reveal a quadrupole pattern in the  $k$ - $\mu$  plane which is due to their impact on the redshift space distortion effect ( $\Omega_m$  determines the growth rate  $f = d \log D_+ / d \log a$ , and  $b$  and  $f$  directly determine the RSD effect in the Kaiser formula).



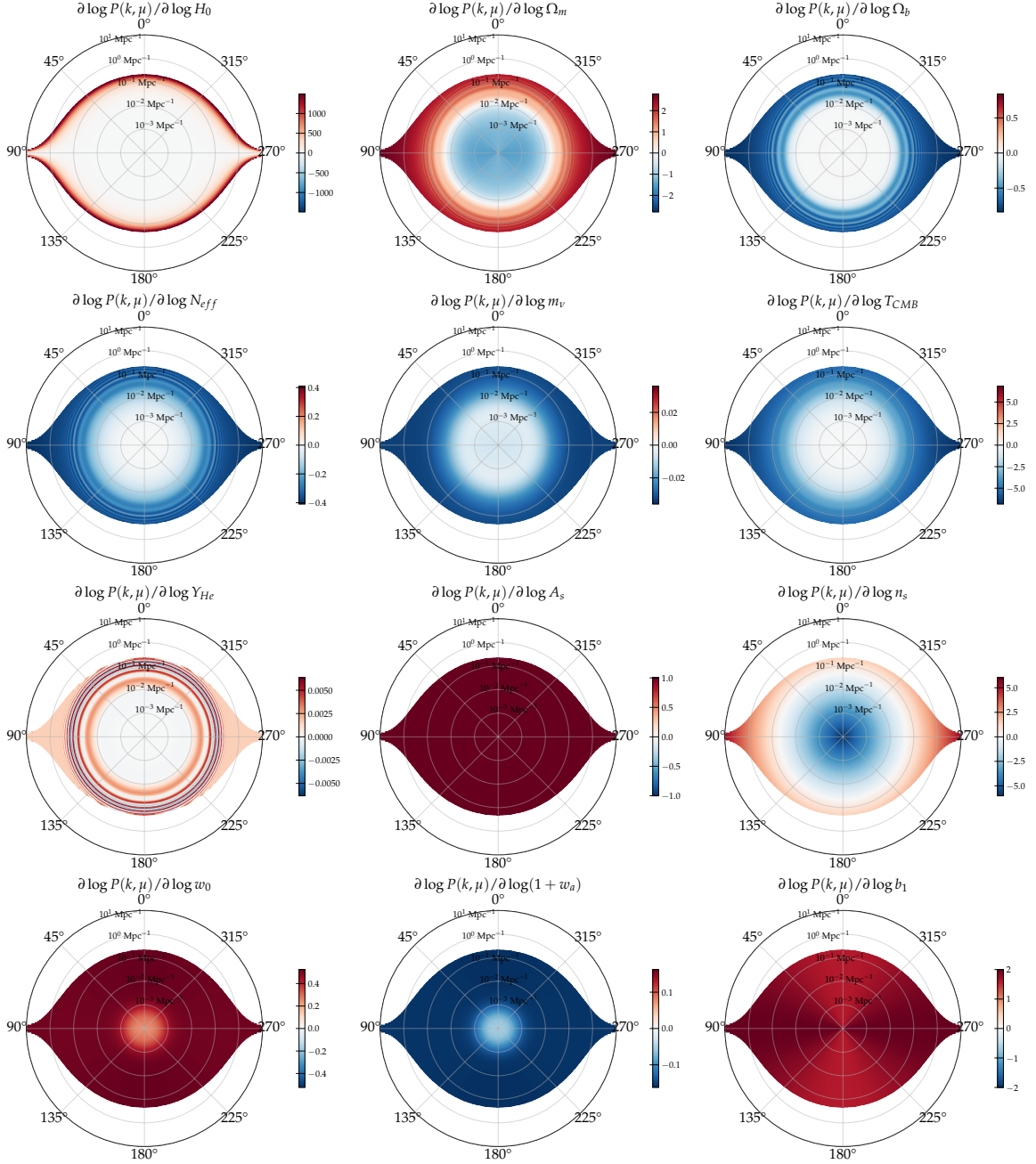


**Figure 5:** Logarithmic derivatives of the two-dimensional redshift-space matter power spectrum w.r.t. model parameters  $\vartheta$ ,  $\partial \log P_{\text{obs}}(k, \mu) / \partial \log \vartheta_i$ . We assume here a redshift error of  $\sigma_{z,0} = 0.03$  which causes the information content to vanish in the white region. The angular coordinate in each plot is the angle between a mode  $\mathbf{k}$  and the line-of-sight, while the radial coordinate is  $k$ , which is clipped to be between  $k_{\text{min}} = 10^{-4} \text{ Mpc}^{-1}$  (the center point) and  $k_{\text{max}} = 10 \text{ Mpc}^{-1}$  (the outer circle). The colour scale indicates a relative increase (red) vs. decrease (blue).

### 4.1.2 Correlation function multipoles

Redshift space distortions on large scales are conveniently expressed in terms of a multipole expansion of the spectrum. These redshift-space power spectrum multipoles are commonly defined as the following expansion in Legendre polynomials [53, 54]

$$P_\ell(k; z) = \frac{2\ell + 1}{2} \int_{-1}^1 d\mu P(k, \mu; z) L_\ell(\mu), \quad (4.5)$$

where  $\mu = \cos \alpha$  is the cosine of the angle  $\alpha$  between the wave vector  $\mathbf{k}$  and the line-of-sight direction  $\mathbf{n}$ ,  $P(k, \mu; z)$  is the anisotropic power spectrum of the tracer, and  $L_\ell$  is the Legendre polynomial of order  $\ell = 0, 1, 2, \dots$ . Then the redshift-space power spectrum multipoles for the Kaiser formula [49] are given by

$$P_\ell(k; z) := \frac{2\ell + 1}{2} \int_{-1}^{+1} d\mu \left( b \delta_m(k; z) - \frac{\mu^2}{\mathcal{H}} \theta_m(k; z) \right)^2 L_\ell(\mu) \quad (4.6a)$$

and therefore with  $P_{\delta\delta} := \delta_m \delta_m^* = P_m$ ,  $P_{\delta\theta} := \delta_m \theta_m^*$ , and  $P_{\theta\theta} := \theta_m \theta_m^*$  the only non-zero multipoles for the linear Kaiser model are

$$P_0(k; z) = b^2 P_{\delta\delta} - \frac{2b}{3\mathcal{H}} P_{\delta\theta} + \frac{1}{5\mathcal{H}^2} P_{\theta\theta} \quad (4.6b)$$

$$P_2(k; z) = -\frac{4b}{3\mathcal{H}} P_{\delta\theta} + \frac{4}{7\mathcal{H}^2} P_{\theta\theta} \quad (4.6c)$$

$$P_4(k; z) = \frac{8}{35\mathcal{H}^2} P_{\theta\theta}. \quad (4.6d)$$

Finally, the correlation function multipoles are defined in terms of the power spectrum multipoles via the integral

$$\xi_\ell(r; z) = \frac{i^\ell}{2\pi^2} \int_0^\infty dk k^2 P_\ell(k; z) j_\ell(kr), \quad (4.7)$$

where  $j_\ell$  is the spherical Bessel function of order  $\ell$ . These integrals are typically efficiently computed using the FFTLOG method [54, 55], which can be implemented in JAX in a few lines, and thus allows differentiable computation of the correlation function.

We show the resulting derivatives of the monopole, quadrupole, and hexadecapole w.r.t. the baseline cosmological parameters in Figure 6. The respective derivative is indicated by a label in each plot. We have omitted the dark energy parameters here as they predominantly affect the growth history and thus only the normalisation of the correlation function multipoles. Clearly visible are the BAO features in many derivatives (but not all). The calculation in this case was carried out using 512 modes geometrically distributed between  $k = 10^{-5} \text{Mpc}^{-1}$  and  $k = 100 \text{Mpc}^{-1}$  since the FFTLOG transform is relatively noisy with fewer sampling points, and even in this case, some ringing can be observed at  $r \gtrsim 200 \text{Mpc}$ . This could likely be improved by additional tweaks to the FFTLOG method, which goes beyond our minimal FFTLOG implementation, and which we leave for future work.

## 4.2 Fisher-forecasting with differentiable solvers

As a proof-of-concept, we demonstrate an application to compute the Fisher information matrix for forecasting. Fisher forecasts are widely used in cosmology for experimental design

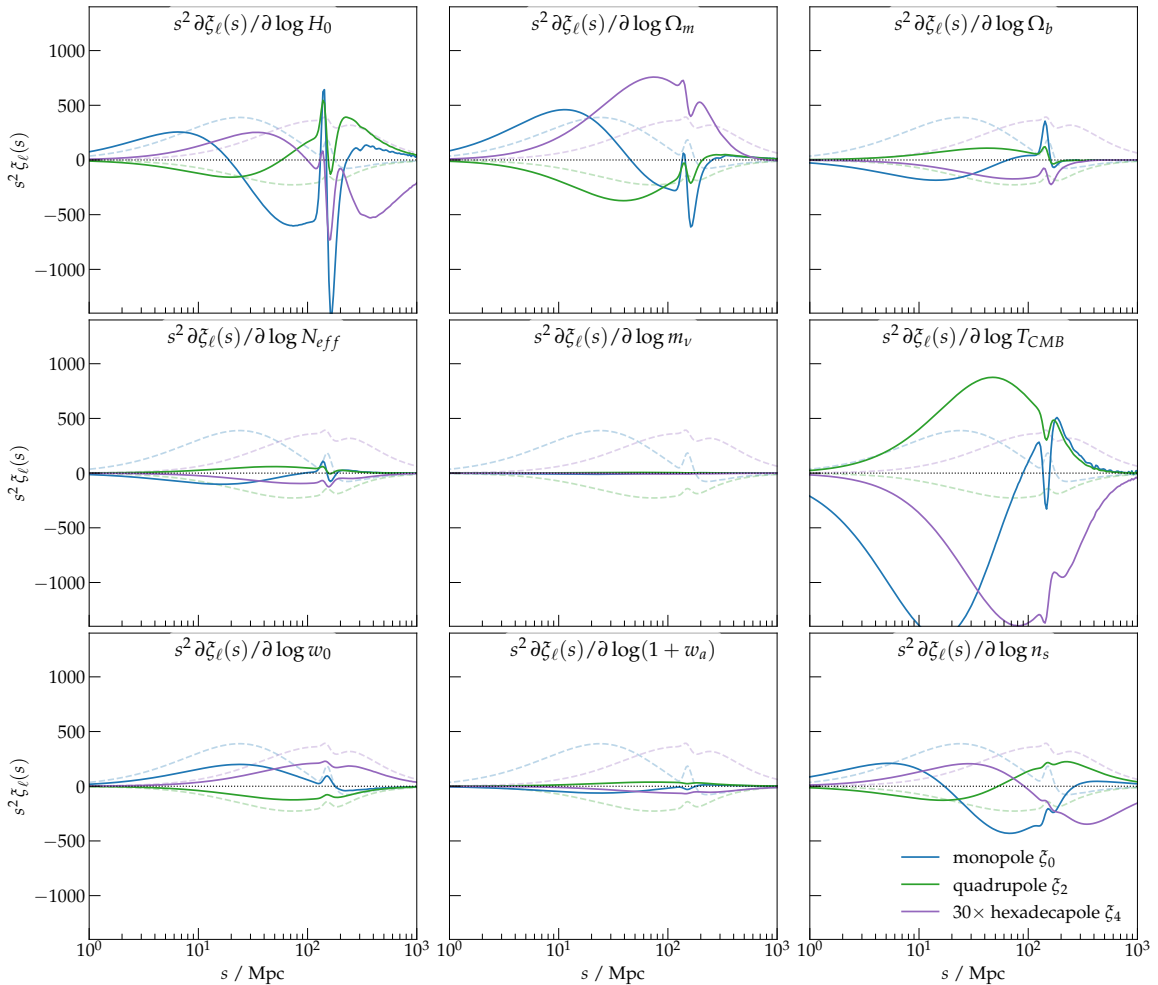


**Figure 6:** Derivative of the redshift-space correlation function multipoles w.r.t. the cosmological parameters. Each panel shows the derivative as a function of scale  $r$  of the monopole  $\xi_0(r)$  (blue), the quadrupole  $\xi_2(r)$  (green), and the hexadecapole  $\xi_4(r)$  (purple), the respective correlation function multipoles (without derivative applied) are shown as light dashed lines. We have multiplied the hexadecapole  $\xi_4$  by a factor of 30 for visual clarity. In this case the derivative is carried through the FFTLOG method and the Einstein-Boltzmann solver.

[56, 57], and they require computing derivatives of the likelihood with respect to the cosmological parameters. Typically, these derivatives are computed with finite differences, which requires careful tuning for convergence [58]. Autodiff makes the computation of the Fisher matrix easier and avoids the convergence problem.

We demonstrate the computation of a Fisher forecast for a photometric Euclid-like survey with 5 bins as described in [50]. For a Gaussian likelihood, the elements of the Fisher matrix for a summary statistic mean  $y(\ell)$  are

$$F_{ij} = \sum_{\ell} \frac{\partial y(\ell)^\top}{\partial \vartheta_i} C^{-1}(\ell) \frac{\partial y(\ell)}{\partial \vartheta_j} \quad (4.8)$$

where  $C(\ell)$  is the covariance matrix computed at the fiducial cosmology. Following [50], we

account for effective bias, anisotropies due to redshift space distortions, and redshift uncertainty in the observed two-dimensional power spectra, given by eq. (4.4). When considering a tomographic survey, the bias parameter  $b_1(z)$  and redshift error,  $\sigma_z(z)$  are of course redshift dependent. Specifically, one has that redshift errors grow roughly like

$$\sigma_z = (1+z)\sigma_{z,0}. \quad (4.9)$$

We used the linear approximation of the covariance matrix [50]:

$$C(\mathbf{k}, \mathbf{k}') \approx \frac{2(2\pi)^2}{V_{\text{eff}}(k, \mu; z)} P_{\text{obs}}^2(k, \mu; z) \delta_D(\mathbf{k} - \mathbf{k}'), \quad (4.10)$$

where  $\delta_D$  is the Dirac delta distribution and  $V_{\text{eff}}$  is the effective volume of the survey given by

$$V_{\text{eff}}(k, \mu; z) = V_s(z) \left[ \frac{n(z)P_{\text{obs}}(k, \mu; z)}{n(z)P_{\text{obs}}(k, \mu; z) + 1} \right]^2 \quad (4.11)$$

with

$$n(z) = \frac{d^2 N(\Omega, z)}{d\Omega dz} \frac{A_{\text{survey}}}{V_s(z)} \Delta z. \quad (4.12)$$

The survey area in the sky is  $A_{\text{survey}} = 15000 \text{ deg}^2$ , and the rest of the parameters are set as in Table 4 in Ref. [50].

The elements of the Fisher matrix are then given by [56, 59]

$$F_{ij}^{\text{bin}} = \frac{1}{8\pi^2} \int_{-1}^1 d\mu \int_{k_{\text{min}}}^{k_{\text{max}}} dk k^2 \frac{\partial \log P_{\text{obs}}(k, \mu; z_{\text{bin}})}{\partial \vartheta_i} \frac{\partial \log P_{\text{obs}}(k, \mu; z_{\text{bin}})}{\partial \vartheta_j} V_{\text{eff}}(k, \mu; z_{\text{bin}}) \quad (4.13)$$

for each tomographic bin. The total Fisher matrix is then computed by summing over the different tomographic bins

$$F_{ij} = \sum_{\text{bin}} F_{ij}^{\text{bin}}. \quad (4.14)$$

Figure 7 shows the resulting Fisher contours, where we used  $k < 0.25 \text{ Mpc}^{-1}$  following the linear case in [50] and computed the power spectra for each tomographic bin at the bin's mean redshift. The Fisher contours agree with the forecast in Fig. 10 in Ref. [50] for galaxy clustering, showing that DISCO-DJ provides exact Fisher matrices and avoids the fine tuning for convergence, which simplifies forecasting. In addition, the Fisher matrix provided by DISCO-DJ is itself differentiable, which allows for optimisation of the figure of merit and easy survey optimisation (see also [32]).

## 5 Summary and Conclusions

In this article, we have presented the Einstein-Boltzmann module of DISCO-DJ (**D**ifferentiable **S**imulations for **C**osmology – **D**one with **J**AX), which implements a differentiable Einstein-Boltzmann solver for cosmological perturbations and will be part of a comprehensive differentiable package for large-scale structure cosmology. DISCO-DJ is based on the JAX library,

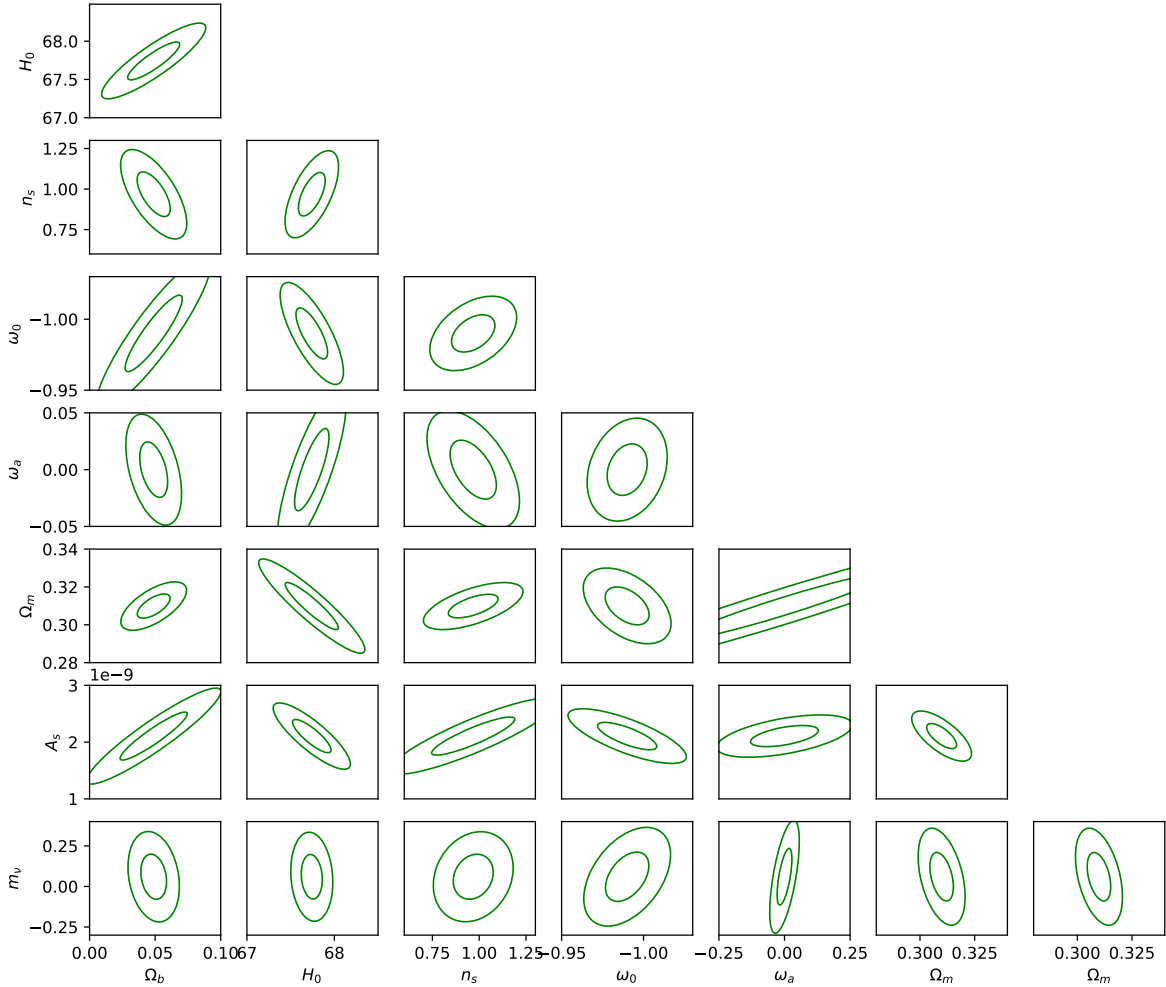


**Figure 7:** 1- and 2- $\sigma$  Fisher contours for a Euclid-like photometric survey. We limited the analysis to with  $k_{\max} < 0.25 \text{ Mpc}^{-1}$ .

which provides automatic differentiation of PYTHON and NUMPY code. Automatic differentiation is a powerful tool for the development of differentiable predictions, as it allows the efficient and accurate computation of derivatives of a model with respect to any input parameter.

In this article, we have introduced the DISCO-DJ Einstein-Boltzmann solver and demonstrated its performance by comparing it to the well-established CAMB and CLASS solvers. Notably, we find that all three solvers typically agree to better than a few per mille when run with high precision settings. We only found some differences in the massive neutrino perturbations in the free-streaming suppressed regime. We have also demonstrated the accuracy of the computation of the Jacobian matrix of the total matter density power spectrum at fixed time with respect to all cosmological model input parameters by comparing it to finite-difference approximations obtained with CAMB and CLASS. We have not (yet) provided a detailed comparison of the computational performance of the autodiff and finite difference approaches, since this would require an optimization of parameters and settings for each code given a desired target accuracy, which is beyond the scope of this paper.

In Section 4, we have demonstrated the power of differentiable solvers by computing

the Jacobian matrix of the total matter density power spectrum at fixed time with respect to all cosmological model input parameters. We have also shown the full time and space dependence of the derivative of the total matter power spectrum w.r.t. the model parameters. We have validated the correctness of the Jacobian matrix by comparing it to finite-difference approximations. We have demonstrated the power of differentiable solvers by computing the Jacobian matrix of the total matter density power spectrum at fixed time with respect to all cosmological model input parameters. We have also shown the full time and space dependence of the derivative of the total matter power spectrum w.r.t. the model parameters. We have validated the correctness of the Jacobian matrix by comparing it to finite-difference approximations.

The output of an Einstein-Boltzmann solver is typically the input for predictions of the summary statistic of an observable. To demonstrate how easy it is to compute such predictions with differentiable solvers, we have computed the redshift-space power spectrum and the correlation function multipoles of biased tracers. We have also demonstrated the computation of a Fisher forecast for a Euclid-like survey. While state-of-the-art modelling would have to take into account also non-linearities and other effects, these results serve as proof-of-concept use cases for our differentiable Einstein-Boltzmann solver.

By visualisation of parameter gradients of a model, we see value also of differentiable solvers for educational purposes as they are capable of directly showing the impact of changes in the (cosmological) model parameters on the observables.

Beyond the applications shown here, we believe that a differentiable Einstein-Boltzmann solver will be useful for more efficient likelihood maximization and sampling, the development of likelihood-free inference methods, and in particular the development of differentiable non-linear models, such as differentiable  $N$ -body solvers, or differentiable non-linear perturbation theory, based on e.g. the effective field theory of LSS (see e.g. [60] for a review) or high-order Lagrangian perturbation theory (e.g. [61, 62]). We expect that they also allow the development of more efficient emulators based on Einstein-Boltzmann solvers [63–66], as they allow inclusion of information from the derivatives of the power spectrum with respect to the cosmological model parameters when building the emulator and should thus require much fewer training points. Naturally, the gradient information can be made part of the emulator itself (such as [67]), which would allow for usage of gradient information in the inference process.

DISCO-DJ is a work in progress, and we plan to extend it in several directions. Most importantly, this module will serve as the starting point for a comprehensive differentiable package for large-scale structure cosmology, which will include a differentiable  $n$ -th order Lagrangian perturbation theory (LPT) module, as well as an  $N$ -body code. Several papers in this direction are currently in preparation. We also invite the community to extend the Einstein-Boltzmann solver to include non-standard cosmological models, such as modified gravity and alternative dark energy and dark matter models.

We will make DISCO-DJ code publicly available upon publication of this paper, while the code is currently available upon reasonable request to the corresponding author.

## Acknowledgments

The authors thank Raul Angulo, Mateja Gosenca, Julien Lesgourgues, Antony Lewis, Thomas Montandon, Cristiano Porciani, and Cornelius Rampf for discussions and/or comments on an earlier draft of this paper. The computational results presented have been achieved in

part using the Vienna Scientific Cluster (VSC). The authors declare no conflicts of interest or external support in the preparation of this manuscript.

## References

- [1] E.M. Lifshitz, *On the gravitational stability of the expanding universe*, *Zhurnal Eksperimentalnoi i Teoreticheskoi Fiziki* **16** (1946) 587.
- [2] E.M. Lifshitz and I.M. Khalatnikov, *Investigations in relativistic cosmology*, *Advances in Physics* **12** (1963) 185.
- [3] S. Weinberg, *Gravitation and Cosmology: Principles and Applications of the General Theory of Relativity*, Wiley (1972).
- [4] P. Peebles, *The Large-scale Structure of the Universe*, Princeton Series in Physics, Princeton University Press (1980).
- [5] C.-P. Ma and E. Bertschinger, *Cosmological Perturbation Theory in the Synchronous and Conformal Newtonian Gauges*, *ApJ* **455** (1995) 7 [[astro-ph/9506072](#)].
- [6] F. Bernardeau, S. Colombi, E. Gaztañaga and R. Scoccimarro, *Large-scale structure of the Universe and cosmological perturbation theory*, *Phys. Rep.* **367** (2002) 1 [[astro-ph/0112551](#)].
- [7] R.E. Angulo and O. Hahn, *Large-scale dark matter simulations*, *Living Reviews in Computational Astrophysics* **8** (2022) 1 [[2112.05165](#)].
- [8] U. Seljak and M. Zaldarriaga, *A Line-of-Sight Integration Approach to Cosmic Microwave Background Anisotropies*, *ApJ* **469** (1996) 437 [[astro-ph/9603033](#)].
- [9] C.L. Bennett, M. Bay, M. Halpern, G. Hinshaw, C. Jackson, N. Jarosik et al., *The Microwave Anisotropy Probe Mission*, *ApJ* **583** (2003) 1 [[astro-ph/0301158](#)].
- [10] Planck Collaboration, P.A.R. Ade, N. Aghanim, M. Arnaud, M. Ashdown, J. Aumont et al., *Planck early results. I. The Planck mission*, *A&A* **536** (2011) A1 [[1101.2022](#)].
- [11] A. Lewis, A. Challinor and A. Lasenby, *Efficient Computation of Cosmic Microwave Background Anisotropies in Closed Friedmann-Robertson-Walker Models*, *ApJ* **538** (2000) 473 [[astro-ph/9911177](#)].
- [12] J. Lesgourgues, *The Cosmic Linear Anisotropy Solving System (CLASS) I: Overview*, *arXiv e-prints* (2011) [arXiv:1104.2932](#) [[1104.2932](#)].
- [13] D. Blas, J. Lesgourgues and T. Tram, *The Cosmic Linear Anisotropy Solving System (CLASS). Part II: Approximation schemes*, *J. Cosmology Astropart. Phys.* **2011** (2011) 034 [[1104.2933](#)].
- [14] M. Bucher, K. Moodley and N. Turok, *General primordial cosmic perturbation*, *Phys. Rev. D* **62** (2000) 083508 [[astro-ph/9904231](#)].
- [15] B. Hu, M. Raveri, N. Frusciante and A. Silvestri, *Effective field theory of cosmic acceleration: An implementation in CAMB*, *Phys. Rev. D* **89** (2014) 103530 [[1312.5742](#)].
- [16] M. Zumalacárregui, E. Bellini, I. Sawicki, J. Lesgourgues and P.G. Ferreira, *hi\_class: Horndeski in the Cosmic Linear Anisotropy Solving System*, *J. Cosmology Astropart. Phys.* **2017** (2017) 019 [[1605.06102](#)].
- [17] A. Zucca, L. Pogosian, A. Silvestri and G.B. Zhao, *MGCAMB with massive neutrinos and dynamical dark energy*, *J. Cosmology Astropart. Phys.* **2019** (2019) 001 [[1901.05956](#)].
- [18] R. Hlozek, D. Grin, D.J.E. Marsh and P.G. Ferreira, *A search for ultralight axions using precision cosmological data*, *Phys. Rev. D* **91** (2015) 103512 [[1410.2896](#)].
- [19] H. Foidl and T. Rindler-Daller, *Cosmological structure formation in complex scalar field dark matter versus real ultralight axions: A comparative study using CLASS*, *Phys. Rev. D* **105** (2022) 123534 [[2203.09396](#)].

- [20] J.C. Hill, E. McDonough, M.W. Toomey and S. Alexander, *Early dark energy does not restore cosmological concordance*, *Phys. Rev. D* **102** (2020) 043507 [2003.07355].
- [21] Google Inc., “Jax: High-performance array computing.” <https://jax.readthedocs.io> Last accessed on 2023-07-20.
- [22] P. Kidger, *On neural differential equations*, Ph.D. thesis, University of Oxford, 2021.
- [23] G.W. Pettinari, C. Fidler, R. Crittenden, K. Koyama and D. Wands, *The intrinsic bispectrum of the cosmic microwave background*, *J. Cosmology Astropart. Phys.* **2013** (2013) 003 [1302.0832].
- [24] R.E. Wengert, *A simple automatic derivative evaluation program*, *Commun. ACM* **7** (1964) 463–464.
- [25] W.R. Inc., “Mathematica, Version 13.3.”
- [26] A. Meurer, C.P. Smith, M. Paprocki, O. Čertík, S.B. Kirpichev, M. Rocklin et al., *Sympy: symbolic computing in python*, *PeerJ Computer Science* **3** (2017) e103.
- [27] D. Onken and L. Ruthotto, *Discretize-optimize vs. optimize-discretize for time-series regression and continuous normalizing flows*, *Preprint* (2020) [2005.13420].
- [28] J. Heek, A. Levskaya, A. Oliver, M. Ritter, B. Rondepierre, A. Steiner et al., *Flax: A neural network library and ecosystem for JAX*, 2023.
- [29] M.C. Kaymak, S.S. Schoenholz, E.D. Cubuk, K.A. O’Hearn, K.M. Merz Jr and H.M. Aktulga, *End-to-end differentiable reactive molecular dynamics simulations using jax*, in *International Conference on High Performance Computing*, pp. 202–219, Springer, 2023.
- [30] D. Phan, N. Pradhan and M. Jankowiak, *Composable effects for flexible and accelerated probabilistic programming in numpyro*, *arXiv preprint arXiv:1912.11554* (2019) [1912.11554].
- [31] E. Bingham, J.P. Chen, M. Jankowiak, F. Obermeyer, N. Pradhan, T. Karaletsos et al., *Pyro: Deep universal probabilistic programming*, *J. Mach. Learn. Res.* **20** (2019) 28:1.
- [32] J.-E. Campagne, F. Lanusse, J. Zuntz, A. Boucaud, S. Casas, M. Karamanis et al., *Jax-cosmo: An end-to-end differentiable and gpu accelerated cosmology library*, *Preprint* (2023) [2302.05163].
- [33] D. Piras and A. Spurio Mancini, *CosmoPower-JAX: high-dimensional Bayesian inference with differentiable cosmological emulators*, *The Open Journal of Astrophysics* **6** (2023) 20 [2305.06347].
- [34] Y. Li, L. Lu, C. Modi, D. Jamieson, Y. Zhang, Y. Feng et al., *pmwd: A Differentiable Cosmological Particle-Mesh N-body Library*, *Preprint* (2022) arXiv:2211.09958 [2211.09958].
- [35] X. Li, R. Mandelbaum, M. Jarvis, Y. Li, A. Park and T. Zhang, *A Differentiable Perturbation-based Weak Lensing Shear Estimator*, *Preprint* (2023) [2309.06506].
- [36] D. Stevanovich, A.P. Hearin and D. Nagai, *A differentiable model of the evolution of dark matter halo concentration*, *Preprint* (2023) [2309.07854].
- [37] E. Hairer and G. Wanner, *Solving Ordinary Differential Equations II: Stiff and Differential-Algebraic Problems*, Springer Series in Computational Mathematics, Springer Berlin Heidelberg (2010).
- [38] S. Nadkarni-Ghosh and A. Refregier, *The Einstein-Boltzmann equations revisited*, *MNRAS* **471** (2017) 2391 [1612.06697].
- [39] J. Lesgourgues and T. Tram, *The Cosmic Linear Anisotropy Solving System (CLASS) IV: efficient implementation of non-cold relics*, *J. Cosmology Astropart. Phys.* **2011** (2011) 032 [1104.2935].



- [40] A. Kværnø, *Singly diagonally implicit runge–kutta methods with an explicit first stage*, *BIT Numerical Mathematics* **44** (2004) 489.
- [41] C. Howlett, A. Lewis, A. Hall and A. Challinor, *CMB power spectrum parameter degeneracies in the era of precision cosmology*, *J. Cosmology Astropart. Phys.* **2012** (2012) 027 [[1201.3654](#)].
- [42] S. Seager, D.D. Sasselov and D. Scott, *A New Calculation of the Recombination Epoch*, *ApJ* **523** (1999) L1 [[astro-ph/9909275](#)].
- [43] P.J.E. Peebles, *Recombination of the Primeval Plasma*, *ApJ* **153** (1968) 1.
- [44] J. Chluba and R.M. Thomas, *Towards a complete treatment of the cosmological recombination problem*, *MNRAS* **412** (2011) 748 [[1010.3631](#)].
- [45] Y. Ali-Haïmoud and C.M. Hirata, *HyRec: A fast and highly accurate primordial hydrogen and helium recombination code*, *Phys. Rev. D* **83** (2011) 043513 [[1011.3758](#)].
- [46] N. Lee and Y. Ali-Haïmoud, *HYREC-2: A highly accurate sub-millisecond recombination code*, *Phys. Rev. D* **102** (2020) 083517 [[2007.14114](#)].
- [47] Planck Collaboration, N. Aghanim, Y. Akrami, M. Ashdown, J. Aumont, C. Baccigalupi et al., *Planck 2018 results. VI. Cosmological parameters*, *A&A* **641** (2020) A6 [[1807.06209](#)].
- [48] V. Desjacques, D. Jeong and F. Schmidt, *Large-scale galaxy bias*, *Phys. Rep.* **733** (2018) 1 [[1611.09787](#)].
- [49] N. Kaiser, *Clustering in real space and in redshift space*, *MNRAS* **227** (1987) 1.
- [50] Euclid Collaboration, A. Blanchard, S. Camera, C. Carbone, V.F. Cardone, S. Casas et al., *Euclid preparation. VII. Forecast validation for Euclid cosmological probes*, *A&A* **642** (2020) A191 [[1910.09273](#)].
- [51] J.A. Peacock and S.J. Dodds, *Reconstructing the Linear Power Spectrum of Cosmological Mass Fluctuations*, *MNRAS* **267** (1994) 1020 [[astro-ph/9311057](#)].
- [52] J. Chaves-Montero, R.E. Angulo and C. Hernández-Monteagudo, *The effect of photometric redshift uncertainties on galaxy clustering and baryonic acoustic oscillations*, *MNRAS* **477** (2018) 3892 [[1610.09688](#)].
- [53] S. Cole, K.B. Fisher and D.H. Weinberg, *Fourier Analysis of Redshift Space Distortions and the Determination of Omega*, *MNRAS* **267** (1994) 785 [[astro-ph/9308003](#)].
- [54] A.J.S. Hamilton, *Uncorrelated modes of the non-linear power spectrum*, *MNRAS* **312** (2000) 257 [[astro-ph/9905191](#)].
- [55] J.D. Talman, *Numerical Fourier and Bessel Transforms in Logarithmic Variables*, *Journal of Computational Physics* **29** (1978) 35.
- [56] M. Tegmark, *Measuring Cosmological Parameters with Galaxy Surveys*, *Phys. Rev. Lett.* **79** (1997) 3806 [[astro-ph/9706198](#)].
- [57] L. Amendola, S. Appleby, D. Bacon, T. Baker, M. Baldi, N. Bartolo et al., *Cosmology and Fundamental Physics with the Euclid Satellite*, *Living Reviews in Relativity* **16** (2013) 6 [[1206.1225](#)].
- [58] N. Bhandari, C.D. Leonard, M.M. Rau and R. Mandelbaum, *Fisher Matrix Stability*, *arXiv e-prints* (2021) arXiv:2101.00298 [[2101.00298](#)].
- [59] H.-J. Seo and D.J. Eisenstein, *Probing Dark Energy with Baryonic Acoustic Oscillations from Future Large Galaxy Redshift Surveys*, *ApJ* **598** (2003) 720 [[astro-ph/0307460](#)].
- [60] M.M. Ivanov, *Effective Field Theory for Large Scale Structure*, *arXiv e-prints* (2022) arXiv:2212.08488 [[2212.08488](#)].
- [61] C. Rampf and O. Hahn, *Shell-crossing in a  $\Lambda$ CDM Universe*, *MNRAS* **501** (2021) L71 [[2010.12584](#)].

- [62] F. Schmidt, *An  $n$ -th order Lagrangian forward model for large-scale structure*, *J. Cosmology Astropart. Phys.* **2021** (2021) 033 [2012.09837].
- [63] G. Aricò, R.E. Angulo and M. Zennaro, *Accelerating Large-Scale-Structure data analyses by emulating Boltzmann solvers and Lagrangian Perturbation Theory*, *arXiv e-prints* (2021) arXiv:2104.14568 [2104.14568].
- [64] M. Bonici, L. Biggio, C. Carbone and L. Guzzo, *Fast emulation of two-point angular statistics for photometric galaxy surveys*, *arXiv e-prints* (2022) arXiv:2206.14208 [2206.14208].
- [65] A. Spurio Mancini, D. Piras, J. Alsing, B. Joachimi and M.P. Hobson, *COSMOPOWER: emulating cosmological power spectra for accelerated Bayesian inference from next-generation surveys*, *MNRAS* **511** (2022) 1771 [2106.03846].
- [66] J. Donald-McCann, F. Beutler, K. Koyama and M. Karamanis, *MATRYOSHKA: halo model emulator for the galaxy power spectrum*, *MNRAS* **511** (2022) 3768 [2109.15236].
- [67] M. Bonici, F. Bianchini and J. Ruiz-Zapatero, *Capse.jl: efficient and auto-differentiable CMB power spectra emulation*, *arXiv e-prints* (2023) arXiv:2307.14339 [2307.14339].
- [68] G. Ballesteros and J. Lesgourgues, *Dark energy with non-adiabatic sound speed: initial conditions and detectability*, *J. Cosmology Astropart. Phys.* **2010** (2010) 014 [1004.5509].
- [69] M. Chevallier and D. Polarski, *Accelerating Universes with Scaling Dark Matter*, *International Journal of Modern Physics D* **10** (2001) 213 [gr-qc/0009008].
- [70] E.V. Linder, *Exploring the Expansion History of the Universe*, *Phys. Rev. Lett.* **90** (2003) 091301 [astro-ph/0208512].

## A Governing equations

In the DISCO-DJ Einstein-Boltzmann solver, we currently implement the linearised equations for perturbations of the metric, as well as CDM, baryons, relativistic species, massive neutrinos, and a dark energy fluid, which we briefly summarise here. Specifically we have implemented the following set of equations, in the *synchronous* gauge, that we reproduce here for reference. We largely follow [5] and use their notation, except that we denote derivatives w.r.t. conformal time by a dash rather than a dot.

**Metric perturbations.** In the synchronous gauge, coordinates are defined by freely falling observers, and scalar metric perturbations are described by two scalar potentials  $\eta$  and  $h$ , cf. [5]. Their evolution is governed by the Einstein equations, which in Fourier space read

$$k^2\eta - \frac{1}{2}\mathcal{H}h' = 4\pi G a^2 \delta T_0^0 \quad (\text{A.1a})$$

$$k^2\eta' = 4\pi G a^2 (\bar{\rho} + \bar{P}) \theta \quad (\text{A.1b})$$

$$h'' + 2\mathcal{H}h' - 2k^2\eta = -8\pi G a^2 \delta T_i^i \quad (\text{A.1c})$$

$$h'' + 6\eta'' + 2\mathcal{H}(h' + 6\eta') - 2k^2\eta = -24\pi G a^2 (\bar{\rho} + \bar{P}) \sigma. \quad (\text{A.1d})$$

These equations are overdetermined so that e.g.  $h'$  is not a dynamical degree of freedom.

**CDM.** As coordinates are defined by freely falling observers, the equations of motion of collisionless cold dark matter are particularly simple:

$$\delta'_c = -\frac{h'}{2} \quad (\text{A.2a})$$

$$\theta_c = \sigma_c = 0. \quad (\text{A.2b})$$

**Baryons.** In contrast, baryons have a finite sound speed and couple to the photons via Thomson scattering while free electrons are present. The temperature and ionization state are determined at the background level by the thermal history solver. The baryon equations of motion (EOMs) are then given by

$$\delta'_b = -\theta_b - \frac{h'}{2} \quad (\text{A.3a})$$

$$\theta'_b = -\mathcal{H}\theta_b + c_s^2 k^2 \delta_b + \frac{4}{3} \frac{\bar{\rho}_\gamma}{\bar{\rho}_b} a n_e \sigma_T (\theta_\gamma - \theta_b) \quad (\text{A.3b})$$

where  $n_e$  is the homogeneous mean electron density,  $\sigma_T$  is the Thomson scattering cross section, and  $c_s$  the adiabatic sound speed of the baryon fluid. The latter is given by

$$c_s^2 = \frac{k_B T_b}{\mu} \left( 1 - \frac{1}{3} \frac{d \log T_b}{d \log a} \right) \quad (\text{A.3c})$$

where

$$T'_b = -2\mathcal{H}T_b + \frac{8}{3} \frac{\mu}{m_e} \frac{\bar{\rho}_\gamma}{\bar{\rho}_b} a n_e \sigma_T (T_\gamma - T_b) \quad (\text{A.3d})$$

is the evolution of the baryon temperature, which explicitly depends on the mean molecular weight  $\mu$  and electron density, which are computed by the recombination solver. The ratio  $\bar{\rho}_\gamma/\bar{\rho}_b$  denotes the photon-to-baryon ratio.

**Photons.** Photons follow Bose-Einstein statistics with two polarisation states, and are coupled to the baryons via Thomson scattering off free electrons. Their EOMs are given by a Boltzmann hierarchy of moments. The first three moments (corresponding to density, velocity, and shear perturbations) are given by

$$\delta'_\gamma = -\frac{4}{3}\theta_\gamma - \frac{2}{3}h' \quad (\text{A.4a})$$

$$\theta'_\gamma = k^2 \left( \frac{1}{4}\delta_\gamma - \sigma_\gamma \right) + a n_e \sigma_T (\theta_b - \theta_\gamma) \quad (\text{A.4b})$$

$$2\sigma'_\gamma = F_\gamma^{(2)'} = \frac{8}{15}\theta_\gamma - \frac{3}{5}kF_\gamma^{(3)} + \frac{4}{15}h' + \frac{8}{5}\eta' - \frac{9}{5}a n_e \sigma_T \sigma_\gamma + \frac{1}{10}a n_e \sigma_T (G_\gamma^{(0)} + G_\gamma^{(2)}) \quad (\text{A.4c})$$

The higher Boltzmann moments for  $\ell_{\max} > \ell \geq 3$  are given by

$$F_\gamma^{(\ell)'} = \frac{k}{2\ell + 1} \left[ \ell F_\gamma^{(\ell-1)} - (\ell + 1) F_\gamma^{(\ell+1)} \right] - a n_e \sigma_T F_\gamma^{(\ell)} \quad (\text{A.4d})$$

and the hierarchy is truncated by hand as in [5] by setting

$$F_\gamma^{(\ell_{\max})'} \approx k F_\gamma^{(\ell_{\max}-1)} - \frac{\ell_{\max} + 1}{\tau} F_\gamma^{(\ell_{\max})} - a n_e \sigma_T F_\gamma^{(\ell_{\max})}. \quad (\text{A.4e})$$

The polarisation moments for  $0 \leq \ell < \ell_{\max}$  are given by

$$G_\gamma^{(\ell)'} = \frac{k}{2\ell+1} \left[ \ell G_\gamma^{(\ell-1)} - (\ell+1) G_\gamma^{(\ell+1)} \right] + an_e \sigma_T \left[ -G_\gamma^{(\ell)} + \frac{1}{2} \left( F_\gamma^{(2)} + F_\gamma^{(0)} + G_\gamma^{(2)} \right) \left( \delta_{\ell 0} + \frac{1}{5} \delta_{\ell 2} \right) \right], \quad (\text{A.4f})$$

(where  $\delta_{\ell j}$  is a Kronecker symbol). The respective hierarchy truncation is given by

$$G_\gamma^{(\ell_{\max})'} \approx k G_\gamma^{(\ell_{\max}-1)} - \frac{\ell_{\max}+1}{\tau} G_\gamma^{(\ell_{\max})} - an_e \sigma_T G_\gamma^{(\ell_{\max})}. \quad (\text{A.4g})$$

**Massless neutrinos.** Massless neutrinos follow Fermi-Dirac statistics, with EOMs given by a Boltzmann hierarchy of moments, of which the first three are

$$\delta'_\nu = -\frac{4}{3} \theta_\nu - \frac{2}{3} h' \quad (\text{A.5a})$$

$$\theta'_\nu = k^2 \left( \frac{1}{4} \delta_\nu - \sigma_\nu \right) \quad (\text{A.5b})$$

$$2\sigma'_\nu = F_\nu^{(2)'} = \frac{8}{15} \theta_\nu - \frac{3}{5} k F_\nu^{(3)} + \frac{4}{15} h' + \frac{8}{5} \eta'. \quad (\text{A.5c})$$

The higher Boltzmann moments for  $3 \leq \ell < \ell_{\max}$  are given by

$$F_\nu^{(\ell)'} = \frac{k}{2\ell+1} \left[ \ell F_\nu^{(\ell-1)} - (\ell+1) F_\nu^{(\ell+1)} \right] \quad (\text{A.5d})$$

with a truncation given by

$$F_\nu^{(\ell_{\max})'} \approx k F_\nu^{(\ell_{\max}-1)} - \frac{\ell_{\max}+1}{\tau} F_\nu^{(\ell_{\max})}. \quad (\text{A.5e})$$

**Massive neutrinos.** Finally, for massive neutrinos, a momentum-dependent Boltzmann hierarchy has to be evolved. This is done by discretising the momentum space into  $n$  bins with momenta  $q \in \{q_0, \dots, q_n\}$ , and evolving the hierarchy for each bin. The moments of the neutrino distribution function  $\psi_q^{(\ell)}$  are then given for each momentum bin, i.e.

$$\psi_q^{(0)'} = -\frac{qk}{\epsilon} \psi_q^{(1)} + \frac{1}{6} h' \frac{d \log f_0}{d \log q}, \quad (\text{A.6a})$$

$$\psi_q^{(1)'} = \frac{qk}{3\epsilon} \left( \psi_q^{(0)} - 2\psi_q^{(2)} \right), \quad (\text{A.6b})$$

$$\psi_q^{(2)'} = \frac{qk}{5\epsilon} \left( 2\psi_q^{(1)} - 3\psi_q^{(3)} \right) - \left( \frac{1}{15} h' + \frac{2}{5} \eta' \right) \frac{d \log f_0}{d \log q}, \quad (\text{A.6c})$$

where  $\epsilon^2 := q^2 + a^2 m_\nu^2$ . The higher Boltzmann moments for  $3 \leq \ell < \ell_{\max}$  are given by

$$\psi_q^{(\ell)'} = \frac{qk}{(2\ell+1)\epsilon} \left( \ell \psi_q^{(\ell-1)} - (\ell+1) \psi_q^{(\ell+1)} \right), \quad (\text{A.6d})$$

and the hierarchy is truncated as

$$\psi_q^{(\ell_{\max})'} \approx \frac{qk}{\epsilon} \psi_q^{(\ell_{\max}-1)} - \frac{\ell_{\max} + 1}{\tau} \psi_q^{(\ell_{\max})} . \quad (\text{A.6e})$$

The massive neutrino perturbations entering the field equations are then given in terms of the lowest moments as

$$\delta\rho_\nu = \frac{4\pi}{a^4} \int dq q^2 \epsilon f_0(q) \psi_0(q) , \quad (\text{A.6f})$$

$$\delta P_\nu = \frac{4\pi}{3a^4} \int dq \frac{q^4}{\epsilon} f_0(q) \psi_1(q) , \quad (\text{A.6g})$$

$$(\bar{\rho}_\nu + \bar{P}_\nu)\theta_\nu = \frac{4\pi k}{a^4} \int dq q^3 f_0(q) \psi_1(q) , \quad (\text{A.6h})$$

$$(\bar{\rho}_\nu + \bar{P}_\nu)\sigma_\nu = \frac{8\pi}{3a^4} \int dq \frac{q^4}{\epsilon} f_0(q) \psi_2(q) , \quad (\text{A.6i})$$

where  $f_0(q)$  is the background neutrino distribution function, which is assumed to be Fermi-Dirac with zero chemical potential. The momentum bins are chosen in order to approximate well these integrals over the Fermi-Dirac distribution, cf. [41] and [subsection 2.4](#).

**Quintessence/dark energy.** Finally, we allow for a dark energy perturbation, which is implemented following [68]. We evolve the following perturbation variables

$$\delta'_Q = -(1+w)(\theta_Q + \frac{1}{2}h') - 3\mathcal{H}(c_a^2 - w)\delta_Q - 9\mathcal{H}(1+w)(c_a^2 - c_w^2)\frac{\theta_Q}{k^2} \quad (\text{A.7a})$$

$$\theta'_Q = -\mathcal{H}(1 - 3c_a^2)\theta_Q + \frac{c_a^2}{1+w}k^2\delta_Q , \quad (\text{A.7b})$$

where we assume the usual (Chevallier-Polarski-Linder [69, 70]) parameterisation of the equation of state parameter  $w := w_0 + w_a(1 - a)$ ,  $c_a^2$  is the (constant) adiabatic sound speed of the dark energy perturbation, and  $c_w^2 := w - w'/(3\mathcal{H}(1+w))$ .

## B Comparison with Class and Camb at early times

In [Figure 8](#), we show the same comparison as in [Figure 2](#), but for  $z = 99$  ( $a = 0.01$ ). The agreement is very good, with the exception of the massive neutrino perturbations where differences are large for wave numbers suppressed by free-streaming damping. Those scales are however dynamically unimportant. Minor differences are seen in the baryon perturbations, likely caused by our simplified thermal history solver. Finally, we see a difference between the CAMB and CLASS cdm+baryon+massive neutrino spectrum for  $k \lesssim 10^{-2} \text{Mpc}^{-1}$ , which is arguably due to differences in how massive neutrinos are weighted in the total matter output spectrum in CLASS compared to CAMB and DISCO-EB.

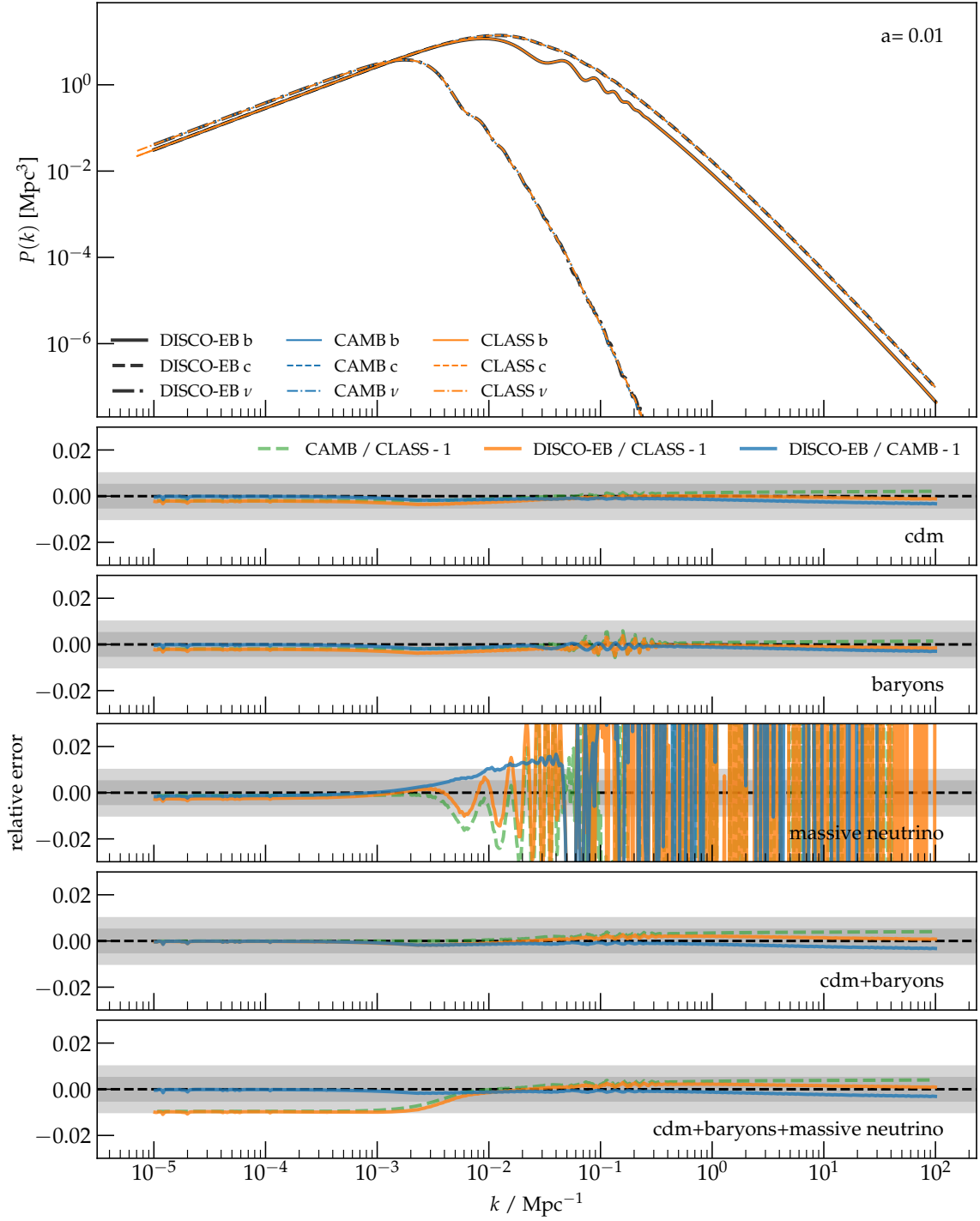


Figure 8: Same as Figure 2, but for  $z = 99$  ( $a = 0.01$ )